Developing the Tools for Effective Quantum Simulation with Trapped Ions

by

George Yang Schwartz

Department of Physics
Duke University

Defense Date: April 1-st, 2025

Approved:

Jungsang Kim, Supervisor

Kenneth Brown

Iman Marvian

Phillip Barbeau

Mark Kruse

Dissertation submitted in partial fulfillment of the requirements for the degree of
Doctor of Philosophy in the Department of Physics
in The Graduate School of Duke University
2025

ABSTRACT

Developing the Tools for Effective Quantum Simulation with Trapped Ions

by

George Yang Schwartz

Department of Physics
Duke University

Defense Date: April 1-st, 2025

Approved:

Jungsang Kim, Supervisor

Kenneth Brown

Iman Marvian

Phillip Barbeau

Mark Kruse

An abstract of a dissertation submitted in partial fulfillment of the requirements for the degree of Doctor of Philosophy in the Department of Physics in The Graduate School of Duke University
2025

Abstract

Atomic trapped ions serve as an excellent platform for quantum simulation and building a future quantum computer. As outlined by David Divencenzo, a viable quantum computer from trapped ions requires a well-characterized atomic qubit, adequate state initialization, long decoherence time, a universal set of gates, and communication between remote sites [DiVincenzo, 2000]. Many of these checkboxes have already been fulfilled from previous groups and will be described in the following chapters. However, if we want to perform quantum simulation, the hardware tools we use need to be improved and refined.

In this thesis, I describe a few tools that I worked on during my tenure as a graduate student to further improve quantum simulation. I discuss efforts towards building an optical cavity around a trapped ion site to improve DiVencenzo's last criterion of communication between remote sites. We explore the operational techniques used in our atomic quantum simulator and improve calibrations to model chemical phenomena. Finally, I look at applying these techniques to simulate the quantum dynamics of a model molecular system.

Trapped ion systems are incredibly versatile, and the possibilities are endless for their future applications. The tools outlined in this thesis help to achieve this potential and set the foundation for future research on quantum dynamics and understanding chemical phenomena.

Dedication

to my Family.

Contents

List of Tables

List of Figures

Acknowledgements

My journey as a doctoral student has been a rocky one, and I would not have been able to complete this work without the support of numerous individuals over the years. First, and foremost, I would like to thank my advisor, Professor Jungsang Kim. Over the years, Jungsang has been very patient with me. Despite where he is in the world, he has made an attempt to have weekly calls to keep track of my progress and answer any questions I may have. His knowledge in optical design was very helpful while we troubleshooted our optical cavity during the Covid pandemic. Although we haven't always seen eye-to-eye, he has provided me with constant financial support so I can continue my research. I would not have been able to write this thesis without his tutelage.

In addition, I would like to thank Professor Kenneth Brown for his help near the end of my PhD. Some of the ideas used to implement the linear vibronic coupling model came directly from my conversations with Ken. When I saw some unusual behavior in my trapped ion simulator, Ken's insight helped me interpret and press forward, even when I had some misgivings about my data. Although I am not his student, I have valued my conversations with him immensely and am always very happy to see him poking around the lab to see how I am progressing.

In the very early years of my PhD, I started under the tutelage of Andre Van Rynbach. Although we overlapped only for a year, Andre taught me some of the fundamentals of ion trapping and optical design. For the next year, I spent some time with Dr. James Joseph. James helped me set up the very early CO_2 ablation set-up, and characterize the first batch of micromirrors. During this time, I also spent time online with the Sandia National Labs team, specifically Christian Arrington and Andrew Hollowell. Both helped me understand the EPICS trap design and were patient with numerous redesigns in the electrode pattern. During the first trapping attempts, I would like to thank Dr. Rachel Noek. Over some extensive calls, she helped set me set up the trap voltage for the EPICs trap and design the early harmonic potentials. I would never have been able to trap in the EPICs chamber without her knowledge.

After the lab moved from Duke main campus to the Chesterfield building, I was able to interact with some of the our teams within Jungsang's group. Dr. Volkan Inlek, the leader of the Cryo team, was always helpful for questions on ion trapping and electrical circuit design. My first trapping success would not have been possible without him. The next year, Dr. Junki Kim became a great friend and mentor to discuss cavity models over lunch. Although he had a separate system to manage, he would find time to overview my set-up and provide new directions for me to take when I was struggling with the system. I also got to spend some time with a new student Ely Novakoski. We were able to troubleshoot our cryogenic system together and it was refreshing to have someone to work a bit closer with.

For the last year of my cavity work, Dr. Geert Vrijsen joined my one-man team. He was already involved in numerous aspects, including but not limited to: helping me set up one of my 370 lasers, working with me to construct the EPICs chamber in the cleanroom, and facilitating my understanding of the underlying physics. Geert and I were able to understand the noise models in our cavity setup and we discussed some of the crucial failings in our design. Discussions with him about his son Wesley were always a wonderful way to start the day and maintain a positive outlook despite struggles in the lab. When my grandma passed on, he was so kind to help me get back on my feet and keep pressing on.

Near the last year of my PhD, I transitioned to the Red Chamber where I joined Ke Sun. Ke was a great mentor, passing on his knowledge of ion trapping, quantum gates and simulation. It was so refreshing to work with a teammate after many years and together we collected the data for our spin-boson paper. He taught me so much about ion trapping, cooling, and gates, ideas I had read on paper but had never implemented in practice. Discussions with him led to most of the work discussed in the final chapter of this thesis. During this time, I also got to work with Mingyu Kang and Hanggai Nuomin. Both helped with modeling our spin boson model, identifying calibration methods, and set the foundation for the Herzberg-Teller chemical model I looked to implement. I also spent some

long calls with Daniel Lobser. Dan was so kind to help fix the RFSoC with me and make sure our IonControl was in working order.

For the last few months of my work, I worked closely with Tinayi (Phoebe) Chen. Together we were able to troubleshoot the headache that is phase tracking in our system and collect meaningful data for both the linear vibronic coupling model and the ISWAP gate. Having her on my team was also great for discussions about system artifacts and how best to proceed during the very last days in our work.

I would also like to thank all the members of the MIST group, both former and current, including Dr. Stephen Crain, Dr. Ye Wang, Chao Fang, Clinton Cahall, Tripp Spivey, Yuhi Aikyo, Jacob Whitlow, Kavya Ranawat, Andrew Van Horn, Marissa D'Onofrio, and Gyeonghun Kim. All were great to have discussions and I feel privileged to have worked with so many brilliant people over the years.

Without the support of my parents, Glen Schwartz and Chihua Yang, I would never have pursued a PhD. They always believed in me and helped foster my curiosity in Physics and research.

During my years at Duke, I have made many lifelong friends who I am forever grateful to and who helped me along this journey. Trevyn Larson, Ethan Arnault and Dripto Debroy, have always supported me and I hope to add one last bottle of champagne to our group. Specifically, Dripto worked with me to edit this thesis and provided valuable feedback on my writing. Another friend Rasheedat Zakare-Fagbamila was also instrumental for emotional support and helping me edit my writing.

Last, but certainly not least, I thank my wife Stephanie Lim. She has been patient with me for a degree that has taken up so many years of our life together. Her love has helped me keep going, no matter how challenging my work was or the mental hurdles I had to overcome. During this past year, after our son Jay was born, she has stepped up to take care of everything at home while I spent long hours in the lab. I would not have been able to write this thesis without her sacrifice and I am so happy she has been a part of my life.

1. Introduction

In 1947, Bell Labs demonstrated the first working transistor. Since then, increasingly powerful computers have been created using this fundamental building block, enabling great breakthroughs in science and engineering. Simultaneously, the transistor density within modern processors doubles approximately every two years, a well-known phenomenon referred to as Moore's law. As transistors continue to miniaturize, nearing the size of angstroms, classical devices are no longer sufficient, and quantum mechanics start to dominate. As such, when we look to the future, a new building block is required.

Furthermore, despite the capabilities of modern computers, there are still some problems in quantum chemistry and biology, for example protein folding, which are completely intractable [Dill and MacCallum, 2012]. Even for simple chemical models such as a two-level system coupled to a bath of harmonic oscillators, known as the Spin-Boson model, the computational complexity grows exponentially with the number of quantum states considered for the spin and the bath [Leggett et al., 1987]. To address Moore's law and simulate nature, Richard Feynman famously said in his 1982 lecture "if you want to make a simulation of nature, you'd better make it quantum mechanical" [Feynman, 1982]. In this thesis, we explore a quantum processor composed of trapped ions.

1.1 Trapped Ions

To create a quantum processor, David DiVincenzo set a list of requirements in 2000: a well-characterized atomic qubit, adequate state initialization, long decoherence time, a universal set of gates, and communication between remote sites DiVincenzo, 2000. Similarly to how the transistor serves as the fundamental building block for modern-day computers, the qubit serves as the building block for quantum computers. Unlike the classical bit, which is restricted to exist in one of two states, 0 or 1, qubits can be superposed in both $|0\rangle$ and $|1\rangle$. We can write the qubit state $|\psi\rangle = \alpha\,|0\rangle + \beta\,|1\rangle$ where α and β are complex numbers that satisfy the relation $|\alpha|^2 + |\beta|^2 = 1$. Without loss in generality, we can write these two terms as $\alpha = \cos(\theta)$ and $\beta = e^{i\phi}\sin\theta$ [Nielsen and Chuang, 2010]. The qubit

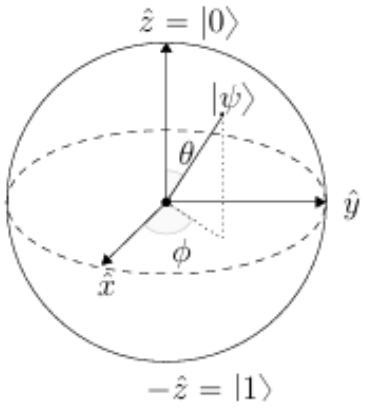

FIGURE 1.1: Bloch Sphere representation of the qubit state ψ.

state vector is best visualized on the Bloch sphere as shown in Figure 1.1.

In addition, qubits share the remarkable feature of entanglement, creating correlations between distant sites that Einstein referred to as "spooky action at a distance" Einstein et al., 1935. These two properties of superposition and entanglement allow a quantum processor to potentially outperform any classical device to solve computational tasks that remain intractable today.

Our qubits of choice are trapped atomic ions. These are by no means the only promising candidate for a quantum processor, with options including superconducting qubits [Devoret and Schoelkopf, 2013] and neutral atoms [Bernien et al., 2017]. However, trapped ions have already been demonstrated to offer excellent control with coherence times far exceeding quantum operations [P. Wang et al., 2021]. The qubit state is encoded into natural occurring atomic energy levels, which we can measure with high precision. Quantum operations can be implemented via precisely shaped optical beams, which we show later in this thesis, to manipulate the atom's quantum state with high fidelity. Photons produced from the atom can be entangled with the atomic state, allowing for communication between remote sites. These characteristics satisfy DiVincenzo's criteria, making trapped ions a fantastic platform for quantum computation and simulation.

Within the alkaline earth metals, many atoms have emerged as potential candidates

for a trapped ion processor, including but not limited to calcium, barium, strontium, and ytterbium. All of these atoms, when ionized, have a single valence electron, making their atomic structure 'hydrogen-like' and simplifying experimental control of the atomic states defined for the qubit. The work contained within this thesis focuses on $^{171}Yb^{+}$, which we will justify later, to carry out experiments.

1.2 Dissertation Overview

This dissertation can best be described in four sections.

1.2.1 Chapter Two

In chapter two, I outline the general framework of atomic ion trapping. I discuss the candidate ion, $^{171}Yb^{+}$, and the benefits of its atomic structure. Furthermore, I discuss how to prepare this qubit, including the cooling methods we employ to lower the atom's phonon state. The chapter concludes with the quantum gates we employ to change the atom's quantum state which we exploit in chapter 5.

1.2.2 Chapter Three

Then, in chapter three, I discuss how we achieve the trapped ion in practice. I discuss the experimental hardware, including how to obtain an Ultra High Vacuum environment for trapping ytterbium. I follow this up with the laser infrastructure we use on a daily basis to trap the atom and control its qubit state. The chapter finishes with characterization measurements to understand our system's capabilities.

1.2.3 Chapter Four

For chapter four, I explore improving the experimental hardware through the incorporation of optical cavities. I discuss the fabrication, testing, and design integration of a cavity design, including novel micromirrors we fabricated to construct microcavities of less than 1 mm. The chapter includes how to couple to these cavities if they are installed in an Ultra High Vacuum environment. I end the chapter with potential faults for future researchers to avoid when incorporating such cavities.

1.2.4 Chapter Five

Lastly, in chapter five, I discuss the implementation of a chemical model, the linear vibronic coupling model, on a trapped ion system. I discuss how this model can be used to witness the Herzberg-Teller effect. I examine the key considerations we take to execute such a model, including careful calibrations of our system, and the results demonstrating the model's behavior on our trapped ion system. I point to limits in our existing calibration methods, and improvements to be made for future work.

2. Trapped Ion Toolkit

The primary ingredient in quantum computing is the qubit, any quantum system with two defined levels that can be controlled, measured, and also isolated from the environment. Trapped ions offer an excellent option as the ions are isolated in an ultra high vacuum (UHV) chamber and their atomic levels are well-defined by nature. Furthermore, to control the atomic state of an ion, we can employ commercially available lasers to change the qubit state and execute quantum computation. In this chapter, we first discuss the theory of how a charged particle can be suspended through the use of static and oscillating electric fields. Then, we will explore our ion of choice and the relevant atomic levels used in order to do quantum computation. Lastly, we will discuss the mechanisms, via quantum gates, available to us to control our now defined qubit which we will employ in more detail in Chapter 5.

2.1 RF Paul Trap

Our first task is to trap a charged particle in space. Unfortunately, due to Earnshaw's theorem, it is impossible to achieve a stable equilibrium using only static electric or magnetic field gradients. This can be written as $\nabla \cdot \vec{E} = 0$, indicating that any electric field lines that point toward a point in space must have the corresponding electric field lines pointing away from the same point in space. The only way to circumvent this issue was proposed by Wolfgang Paul, using a combination of static and dynamic electric fields.

In 1989, Wolfgang Paul received the Nobel Prize for developing a way to suspend 'constituents of matter' without 'material walls' [Paul, 1990]. The concept utilizes a combination of oscillating and static electric fields to confine particles within a three-dimensional trapping region. Specifically, the radio frequency (RF) electric field, typically on the order of tens of MHz, oscillates in the presence of a static field gradient and produces a saddle point as shown in Figure 2.1b. For the rest of this thesis, we will employ a version of Paul's design to trap our ions of interest.

A typical Paul trap contains two rods set to the RF signal and two rods grounded. In

addition, there are two direct current (DC) rods which we will define at voltage U_0 at the endcaps around the ion position. The potential field for this configuration can be described by

$$\Phi(x,y,z,t) = V_0\cos(\Omega t)(1+\frac{y^2-z^2}{R^2}) + \kappa U_0(x^2-\frac{y^2+z^2}{2}) \tag{2.1}$$

where κ is a geometrical factor determined by the trap and R is much larger than the radius of the trap rods. We consider the electric field to be the negative divergence of the potential

$$\vec{E}(x,y,z,t) = -\vec{\nabla}\Phi(x,y,z,t) = V_0\frac{\cos(\Omega t)}{R^2}(2y\hat{y}-2z\hat{z}) + kU_0(2x\hat{x}-y\hat{y}-z\hat{z}). \tag{2.2}$$

Considering just the y and z axes, the equations of motion look like

$$m\ddot{y} = e\vec{E}_y = eV_0\frac{\cos(\Omega t)}{R^2}2y - e\kappa U_0 y \tag{2.3}$$

$$m\ddot{z} = e\vec{E}_z = -eV_0\frac{\cos(\Omega t)}{R^2}2z - e\kappa U_0 z \tag{2.4}$$

where m and e are the mass and charge of the ion respectively. Using dimensionless parameters, we can rewrite these equations in the form of Mathieu equations:

$$\frac{d^2y}{d^2\tau} + [a+2q\cos 2\tau]y = 0 \tag{2.5}$$

$$\frac{d^2z}{d^2\tau} + [a-2q\cos 2\tau]z = 0 \tag{2.6}$$

where we define $\tau \equiv \frac{\Omega t}{2}$, $a \equiv -4\kappa eU_0/m\Omega^2$, $q \equiv 2eV_0/m\Omega^2R^2$. The Mathieu equations, 2.5 and 2.6, can be solved using Floquet solutions[Sträng, 2007] which can be written in a form: [Sun, 2024]

$$u_i(t) \sim A_i\cos\omega_r t[1+\frac{q}{2}\sin\Omega t] \tag{2.7}$$

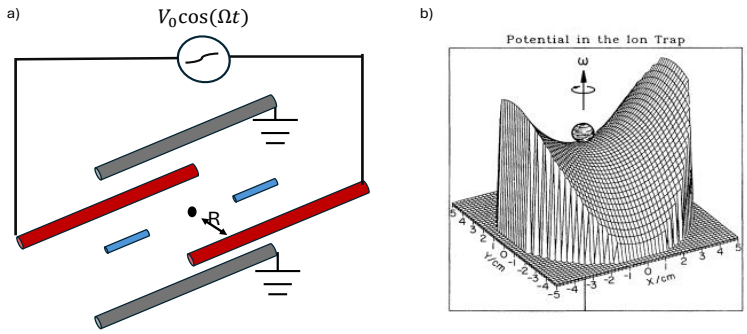

FIGURE 2.1: **Four rod trap with saddle point electric field representation.** a) The four rod trap Geometry. The two red rods are driven with an oscillating RF voltage at frequency Ω and amplitude V_0. The other two grey rods are grounded. At the end caps, around the ion, two DC rods are shown in blue. The rod diameter is very small compared to the distance to the ion R. b) The saddle point potential created from the radio frequency (RF) and static electric field gradients. In reality, the saddle is oscillating at the frequency of the RF, but the local minimum location stays constant. A ball has been placed at this minimum to represent an ion sitting in the saddle point potential. Image taken from[Paul, 1990].

where i can be either the y or z axis, A_i depends on the initial conditions, and the secular frequency (also known as the oscillator frequency or radial mode frequency) is ω_r. Specifically, when $a \ll q^2 \ll 1$, the radial potential is analogous to the frequency in a harmonic potential where $eV_{eff} = \frac{1}{2}m\omega_r^2(y^2 + z^2)$ and the secular frequency is written as [Debnath, 2016]

$$\omega_r = \frac{q\Omega}{2\sqrt{2}} = \frac{eV_0}{\sqrt{2}m\Omega R^2} \tag{2.8}$$

Conducting a similar analysis on the x axis derived from Equation 2.2 gives us the 'axial' mode frequency $\omega_x = \sqrt{2\kappa eU_0/m}$ where $\omega_x \ll \omega_r$ due to the much weaker axial confinement in the trap.

2.1.1 Surface Trap

The four rod trap is an excellent diagnostic method to demonstrate the trapping of atomic ions. However, as quantum processors look to the future, large computations will require hundreds, if not thousands, of ions. Trapping all these ions onto a single trap will cause crosstalk errors between the many modes of collective motion and limit gate speeds to $R_{gate} \sim 1/\sqrt{N}$ where N is the number of ions [Brown et al., 2016]. Separating the ions onto respective trapping sites and then shuttling the information, instead spreading the quantum information via photonic interconnects, would allow quantum computing to scale into the future. These trapping sites need the following requirements: a method to deliver the requisite RF and DC voltages for the trap potential, clear avenues to deliver optical beams for quantum gates (this will be discussed further in Section 2.3.2) and reliable reproducibility. Four rod traps, which are typically hand made, do not offer the precision necessary to satisfy these requirements. Alternatively, silicon CMOS (complementary metal-oxide-semiconductor) technology allows for precise reproducible microfabrication of control electrodes onto a flat platform. These flat traps will henceforth be referred to as 'surface traps.'

In this thesis, the trap diagnostics and quantum simulations were conducted on a surface trap named 'Phoenix' fabricated by Sandia National Laboratories and shown in Figure 2.2a [Revelle, 2020]. The RF and DC electrodes utilized in the four rod trap design have been replaced by gold-patterned electrodes on the top bowtie layer referred to as the trap die. The die is epoxied to an interposer with each respective electrode wire bonded from the die to the interposer at the ends of the bowtie shape. The interposer pins have been connected to a Ceramic Pin Grid Array (CPGA) which can then be connected to a custom printed circuit board (PCB). We discuss the rest of this set-up in our experimental hardware, detailed in Chapter 3. Figure 2.2c and d illustrate the RF null generated from the electrodes. This is the lowest potential point when no DC voltage is applied and is typically located at $y = 0\mu m$ and $z = 68\mu m$ above the trap surface. Although there is some variation in

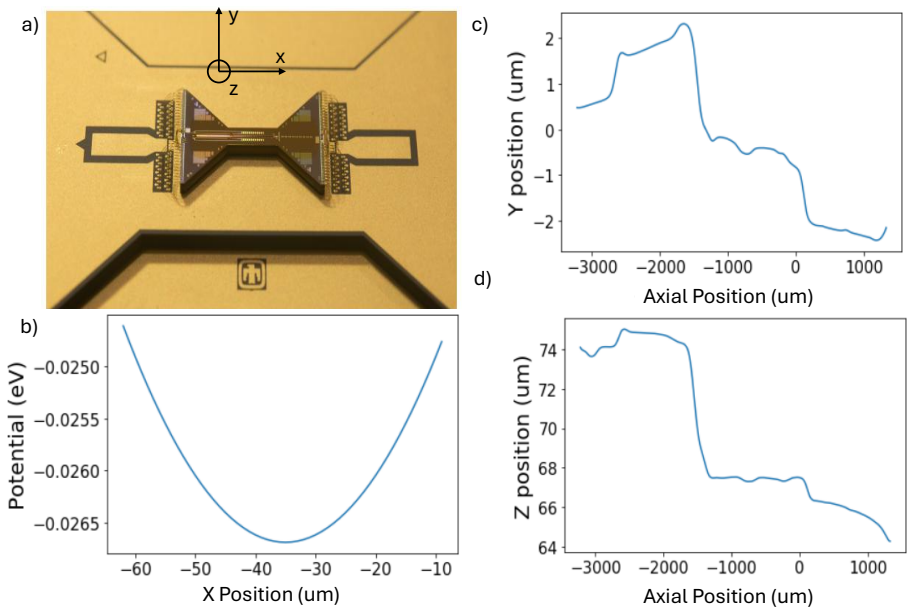

FIGURE 2.2: **Phoenix Trap with simulated trap fields along x, y, and z.** a) Picture of Phoenix trap developed by Revelle, 2020. Two RF tube electrodes travel along the x axis. DC electrodes sandwich around the RF tubes producing potentials along the x and y axis. b) Potential produced by the DC electrodes creates a symmetric axial confinement (x axis). The RF null positions along the axial direction for the y axis (c) and z axis (d).

this location depending on the axial x location, we maintain our ions typically between $x = (-245\mu m, 175\mu m)$, making this null point remain relatively constant. Along the axial direction, the DC voltages produce a symmetric harmonic solution shown in Figure 2.2b.

2.1.2 Motional modes of an ion chain

Up to this point, we have been limiting our discussion to the scenario which we trap one ion in the chamber. When we start to trap multiple ions in a linear chain of ions, the ions repel each other in the form of Coulomb interactions. The Coulomb repulsive forces and the harmonic potential discussed in the previous section can eventually reach an equilibrium, resulting in the ions settling into a set of 'normal modes' for the ion chain.

For a linear n-ion chain along the axial x-direction, the ion chain's potential energy can be described via the sum of the harmonic potential and the repulsive Coulomb interaction

$$V = \frac{1}{2}m\sum_{j=1}^{n}(\omega_x^2 x_j^2 + \omega_y^2 y_j^2 + \omega_z^2 z_j^2) + \frac{e^2}{2}\sum_{i\neq j}\frac{1}{\sqrt{(x_i - x_j)^2 + (y_i - y_j)^2 + (z_i - z_j)^2}} \tag{2.9}$$

where m is the ion's mass, ω_ξ, $\xi \in x, y, z$, are the axial and two radial frequencies respectively, and i and j represent each ion in the chain.

Using the following substitutions for the position variables: $q_{i,x} = x_i - x_j$, $q_{i,y} = y_i$ and $q_{i,z} = z_i$ and diagonalizing the resultant potential, the effective Hamiltonian for the system becomes

$$H = T + V = \sum_{k,\xi}(\frac{1}{2}m\omega_{k,\xi}^2 Q_{k,\xi}^2 + \frac{P_{k,\xi}^2}{2m}) \tag{2.10}$$

where $\omega_{k,\xi}$ represent the collective motional modes. We have defined $Q_{k,\xi}^2 = \sum_j b_{\kappa,\xi}^j q_j$ as the unitary transformed position operator and $P_{k,\xi}^2 = \sum_j b_{\kappa,\xi}^j p_j$ as the transformed momentum operator. This Hamiltonian represent a set of decoupled harmonic oscillators, each with respective mode frequency $\omega_{k,\xi}$ along the ξ-axis. In our experiment, we only concern ourselves with motion along one axis, so we can omit ξ. Furthermore, the coupling strength of each ion, j, to the k^{th} mode is dictated by the b_κ^j. For a 7-ion chain used in our experiment, the contributions of each ion to their respective mode is shown in Figure 2.3. A more detailed derivation can be found in [Zhang, 2021].

2.2 Ytterbium Ion

The natural atomic structure gives us four common methods to encode a qubit: optical qubit, Zeeman qubit, hyperfine qubit, and fine-structure qubit. Of these four, hyperfine qubits are the predominant favorite in the community because of their very high lifetimes and resistance to magnetic-field noise [Bowers et al., 1996]. When selecting a hyperfine qubit, choosing an atom with hydrogen-like atomic level structure makes it simple to identify an ideal two-level system. Common candidates in the community are from the ionized

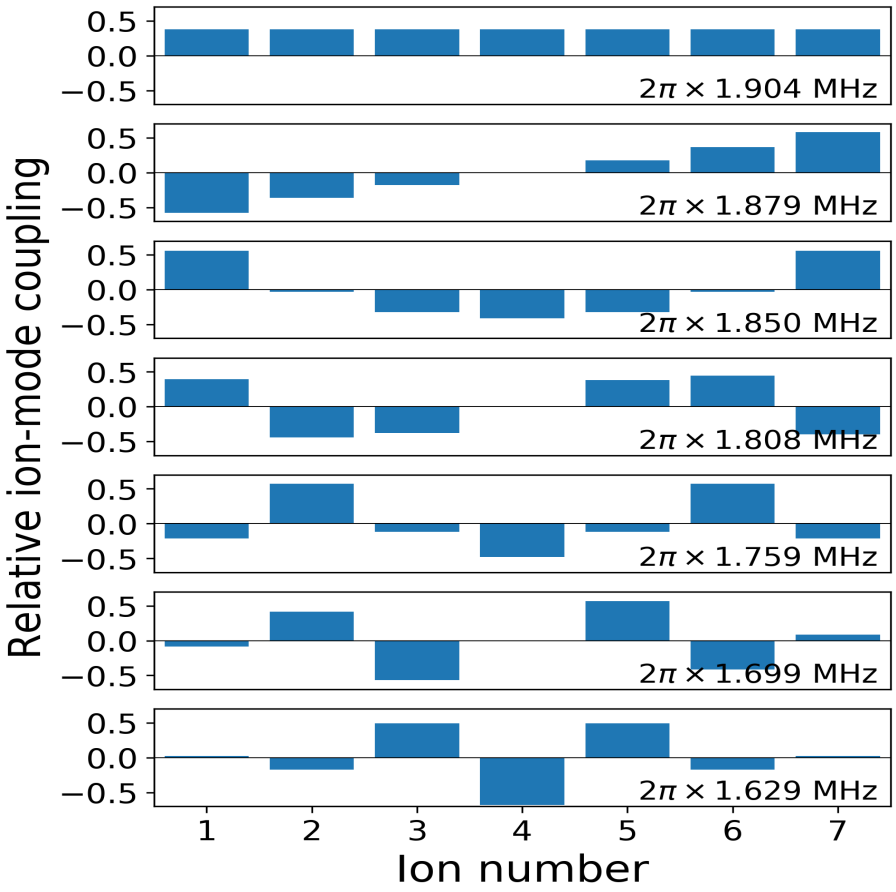

FIGURE 2.3: **Relative ion coupling strength to each normal mode of the ion chain.** The highest frequency mode we refer to the common mode as all the ions couple to it equally. The lowest frequency mode, with each neighbor ion having an opposite coupling direction, we refer to as the zig-zag mode. We use the zig-zag mode for most of our experiments. Motional frequencies were measured on 02-26-2024.

alkaline earth metals: calcium, barium, and strontium. Another candidate, ytterbium, particularly the $^{171}Yb^{+}$ isotope, also emulates the hydrogen structure with the added benefit of a 355 nm Raman transition, which will be discussed later. This wavelength has been engineered for decades making the Ytterbium ion an ideal choice to proceed with.

One crucial metric for quantum information is coherence time. $^{171}Yb^{+}$ has demonstrated remarkable coherence times, ranging from seconds to even hours if one uses dynamical decoupling schemes [P. Wang et al., 2021]. As complex quantum algorithms and computations become longer, this extended coherence time is crucial to perform reliable quantum circuits

with minimal error accumulation.

Besides the accessible Raman transition, $^{171}Yb^{+}$ benefits with its compatibility of existing laser technologies and components. The cycling transition between $2S_{1/2} \rightarrow 2P_{1/2}$ in Ytterbium is at 369.5 nm, a convenient wavelength for laser cooling, state initialization and measurement. This wavelength has commercially available optical components, including but not limited to high frequency free space acoustic-optic and electro-optic modulators, which facilitates researchers aiming to scale a quantum system into the future.

2.2.1 $^{171}Yb^{+}$ Structure

The energy levels of ytterbium have already been clearly identified and verified over the past two decades [Olmschenk et al., 2007]. The key transitions needed to drive quantum operations are shown in Figure 2.4. $^{171}Yb^{+}$ hyperfine levels will be our qubit of choice, where we will define $|1\rangle = \left|F = 1, m_f = 0\right\rangle$ and $|0\rangle = \left|F = 0, m_f = 0\right\rangle$ as our respective bright and dark state. This 'clock' state, as it is often referred to, has an energy separation that is well defined at $12.642812118526GHz + 310.8(B^2)Hz$. B represents the magnetic field, indicating the transition is insensitive to magnetic field fluctuations to first order.

2.2.2 Neutral Flux

There are two predominant methods to create a neutral flux of atoms, oven loading and ablation loading. Perhaps the more conventional method, oven loading requires restively heating a thermal source to generate a sublimated stream of neutral atoms. The downsides of this method are the large heat load required to reach sublimation and the potential risk of trap degradation by depositing neutral Yb metal onto the trap surface. Ablation loading avoids these concerns with the added benefit of an efficient time-to-trap of 9 ms Vrijsen et al., 2019. We create the Yb neutral flux with a 1064 nm ablation laser that is directed over the trap. At the same time, a 399 nm laser, also aligned over the trapping region, is tuned to the $6s^2(^0S_1)$ to $6s6p(^1P_1)$ transition of Yb. By finely tuning the 399 nm wavelength, we can photoionize our choice of isotope, the 174 isotope at 751.52649(0) THz or the 171 isotope at 751.52749(0) THz. Once the electron is in the $6s6p$ state, another wavelength

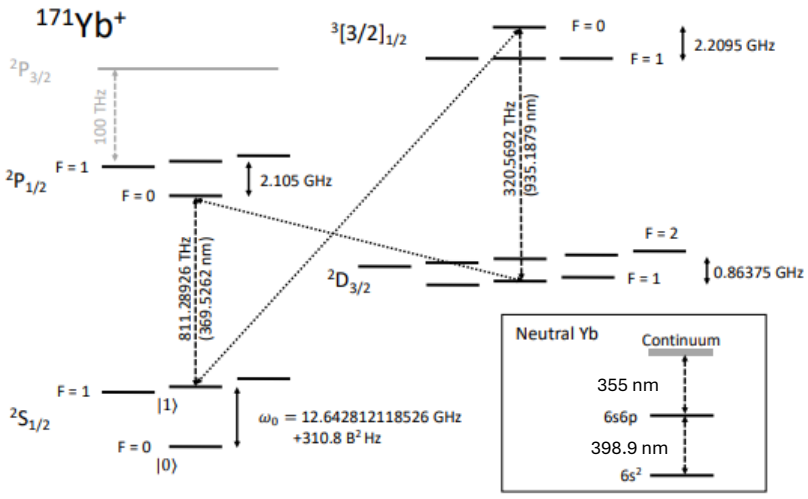

FIGURE 2.4: **Relevant Energy Levels for Ytterbium Qubit Operations.** The inset demonstrates the ionization protocol, using both 355 nm and 398.9 nm, to remove one of the two electrons in the neutral Ytterbium's valence shell.

shorter than 394 nm is needed to push the electron into the continuum. In our setup, we have two available options, the 370 nm cooling laser or the 355 nm Raman laser. Since we have tuned the 370 nm laser power to be below the saturation intensity to optimize Doppler cooling, the natural option is to use the 355 nm laser. Once the ions are loaded, they are confined by the harmonic potential described in Section 2.1.

2.2.3 Cooling, State Initialization and Measurement

After neutral Yb is ionized, the ions have too much kinetic energy to be trapped in the harmonic potential described in 2.1. The $^{171}Yb^{+}$ ion's kinetic energy can be lowered by Doppler cooling the ion using the electric dipole cycling transition $^2S_{1/2} \leftrightarrow^2 P_{1/2}$ at 369.53 nm. The basic intuition of Doppler cooling is using a red-detuned laser from the cycling transition such that only ions flying towards the laser beam are excited via the Doppler effect. These ions absorb a photon from the laser, resulting in a momentum kick $\hbar\vec{k}$ where $\vec{k}$ is the wavevector of the photon. The momentum kick is in the opposite direction of the ion's motion, lowering its kinetic energy. The ion can then spontaneously emit to $^2S_{1/2}$ with a photon emitted in a random direction, which can heat the atom's motion.

The process continues until the absorption-emission system reaches an equilibrium where the final temperature is limited by the natural linewidth of the atomic transition and the photon recoil energy. The prior, referred to as the Doppler temperature, is given by

$$T_{Doppler} = \frac{\hbar\Gamma}{2k_B} \tag{2.11}$$

where k_B is the Boltzmann constant and $\Gamma = 2\pi \times 19.6MHz$ is the natural linewidth of the S to P transition. The latter, known as the recoil temperature, arises due to the random momentum kick experienced due to spontaneous emission and is given by

$$T_{recoil} = \frac{\hbar^2 k^2}{2Mk_B} \tag{2.12}$$

where M is the mass of the ion. In a typical atom like Yb, the recoil temperature limit is lower than the Doppler temperature.

To apply Doppler cooling in practice, we slightly red-detune the 369.53 nm by $\approx 15MHz$ from the cycling transition. The detuning, Δ, is dependent on the photon scattering rate

$$\Gamma_{scattering} = \frac{s}{1 + s + \frac{\Delta^2}{\Gamma^2}} \tag{2.13}$$

where s is the ratio between the intensity and saturation intensity, I_s, given by

$$I_{sat} = \frac{\pi hc\Gamma}{3\lambda^3 R_{br}}. \tag{2.14}$$

For $^{171}Yb^+$, where $\lambda = 369.53nm$ and the branching ratio $R_{br} = 0.995$, the saturation intensity is $I_{sat} = 51mW/cm^2$ [Olmschenk et al., 2007]. In our system, we have an elliptical 369.5 nm beam, $20\mu m \times 60\mu m$, resulting in the approximate saturation intensity at 1.9 μW. In practice, we optimize the Doppler cooling by scanning the 369.53 nm intensity and comparing to the measured phonon counts. If we use our measured radial mode frequency, ω, of approximately $2\pi \times 2$MHz, the average phonon number achievable via Doppler cooling is

$$\bar{n} = \frac{k_B T_{Doppler}}{\hbar\omega} = \frac{\Gamma}{2\omega} \approx 4.9quanta \tag{2.15}$$

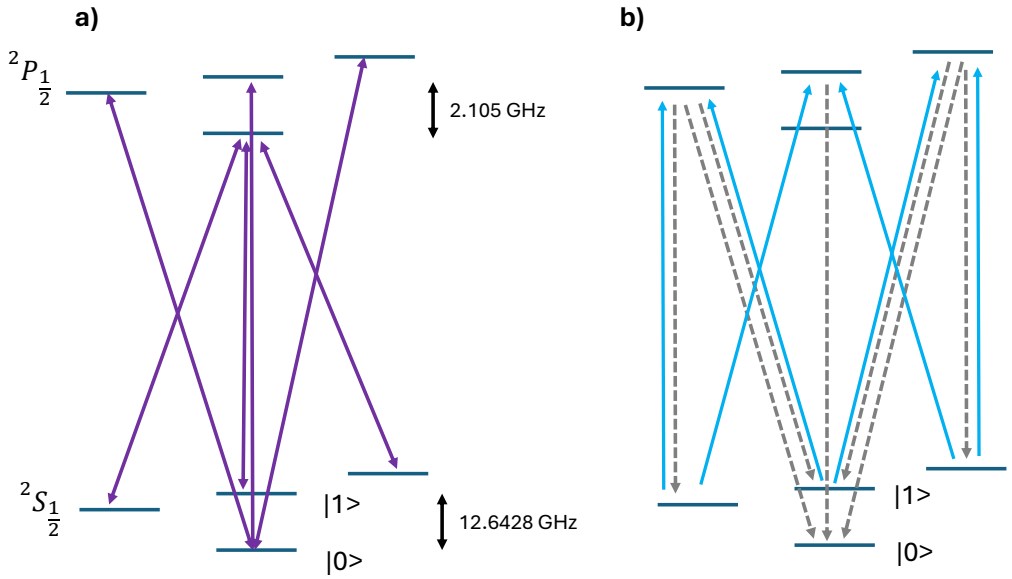

FIGURE 2.5: **Doppler Cooling and Optical Pumping for $^{171}Yb^+$.** a) Doppler cooling mechanism with 14.7 GHz sidebands on the 369.5 nm laser. b) Optical pumping method with possible spontaneous decay pathways (shown in gray) to prepare the ion in the $|0\rangle$ state. The decay into the $^3D_{3/2}$ state is not shown, but is constantly addressed with a 935 nm with a 3.01 GHz sideband.

We also note that the trap potential is set such that the cooling beam is not perpendicular to any of the principle axes of the trap. In this configuration, a single cooling beam can project onto the ion's motion in all directions. Without any modulation, the 369.5 nm laser can only address the direct transition between $^2S_{1/2}\left|F=1,m_f=-1,0,1\right\rangle$ to $^2P_{1/2}\left|F=0\right\rangle$. We apply a 14.7 GHz sideband onto the 369.5 nm laser to also stimulate the transition from $^2S_{1/2}\left|F=0\right\rangle$ to $2P_{1/2}\left|F=1,m_f=-1,0,1\right\rangle$, shown in Figure 2.5 a. Throughout, this whole process, a 935 nm laser with a 3.01 GHz sideband is projected onto the ions, allowing for the D-sublevel to be repumped to the S manifold.

To achieve sub-Doppler temperatures, we utilize two techniques: Electromagnetically-induced transparency (EIT) and sideband cooling.

2.2.3.1 Optical Pumping and Measurement

To initialize the qubit, the quantum state needs to be set to $|0\rangle$. This process is shown in Figure 2.5b for $^{171}Yb^{+}$. The 369.5 nm laser shining on the ion is first propagated through a free-space 2.1 GHz modulator to drive the $^2S_{1/2}\left|F=1,m_f=-1,0,1\right\rangle$ states to the $^2P_{1/2}$ level. Spontaneous emission allows the ion to relax to both the $^2S_{1/2}\left|F=1\right\rangle$ and $^2S_{1/2}\left|F=0\right\rangle$ levels. The pumping continues until the population in the $^2S_{1/2}\left|F=1\right\rangle$ is depleted, which typically takes on the order of a few microseconds.

We can confirm the population during the detection process. For this, the high frequency modulators are turned off, making the only resonant transition between $^2S_{1/2}\left|F=1,m_f=-1,0,1\right\rangle \rightarrow {}^2P_{1/2}\left|F=0\right\rangle$. Spontaneous emission only allows the ion to relax to the $^2S_{1/2}\left|F=1\right\rangle$ manifold because the transition between $^2S_{1/2}\left|F=0\right\rangle$ and $^2P_{1/2}\left|F=0\right\rangle$ is prohibited. Since this transition is closed-loop, it is often referred to as the cycling transition. The proportion of detected photons measured during the detection time identifies the probability of the ion being in the $|1\rangle$ state.

2.2.4 EIT Cooling

Consider a three-level lambda system shown in Figure 2.6a. When a probe beam with frequency ω_p is shined on the ion, it can stimulate a transition from state $|1\rangle$ to $|2\rangle$ if its detuning $\Delta_p = 0$. Increasing this detuning, decreases the likelihood of this transition, and the resultant lineshape as a function of Δ_p is a Lorentzian centered about zero.

When another strong laser beam, which we call the coupling beam, is applied on the resonant transition between $|2\rangle$ and $|3\rangle$, these states become coupled, resulting in a set of dressed states $|2'\rangle$ and $|3'\rangle$. This leads to the probe beam ω_p no longer being resonant with the $|1\rangle$ to $|2\rangle$ transition, or being *transparent* at its original frequency.

By careful adjusting the coupling beam's detuning, we can manipulate the lineshape of these dressed states. Typically, this manipulation is done to create the Fano lineshape shown in Figure 2.6b. This scenario makes the predominant red sideband transition frequency, which lowers the phonon number ($|n\rangle \rightarrow |n-1\rangle$), the primary peak in the spectrum. The

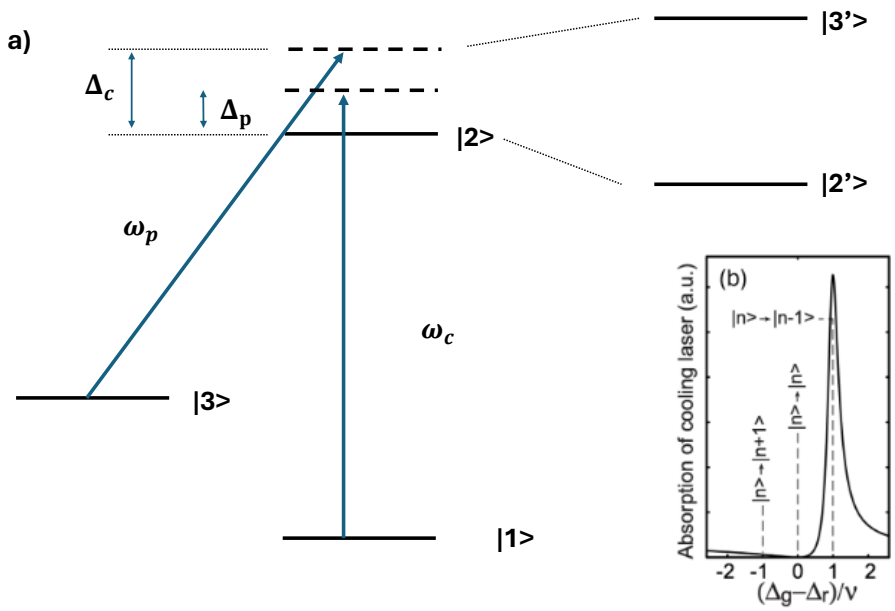

FIGURE 2.6: **Fundamental Diagram of EIT Cooling.** a) A coupling beam ω_c creates two dressed states $|2'\rangle$ and $|3'\rangle$ in a *Lambda* system. The original $|2\rangle$ state then becomes transparent to the probe beam. b) Fano lineshape created when adjusting the detuning of the coupling beam Δ_C. Adapted from [Sun, 2024]

carrier ($|n\rangle \rightarrow |n\rangle$) and blue sideband transition ($|n\rangle \rightarrow |n+1\rangle$) are weakly coupled to, so on average, the phonon number decreases by one with each round of excitation. The cycle ends with a round of spontaneous emission, where the excited state returns to the ground state $|1\rangle$, allowing for the process to continue.

2.2.4.1 Sideband Cooling

The Doppler cooling limit sets $\bar{n} \approx 5$ which is not ideal for quantum simulations. To achieve a lower phonon number, we employ red and blue sideband transitions (RSB and BSB, respectively), which can change the phonon number. This technique can achieve near ground state cooling and we measure $\bar{n} \approx 0.0424$ for the zig-zag mode we use for our quantum circuits.

Sideband cooling drives a coherent red sideband transition followed by optically pumping the qubit to the $|0\rangle$ state. The red sideband transition drives the $|0, m\rangle$ to $|1, m-1\rangle$, removing one motional quanta and bringing the spin to the $|1\rangle$ state. Repumping the ion

with the same 369.5 nm light used in state preparation returns the ion to the $|0\rangle$ state. There is the possibility that the spontaneously emitted photon increases the phonon number by 1, but this scales as the Lamb-Dicke parameter squared [Wu et al., 2023]. Iterating this process can bring the phonon down to $1.25\eta^2$.

We can measure the efficacy of this technique by comparing the populations of driven red and blue sidebands. The probability the ion being in state $|1\rangle$ for a respective red and blue sideband transition are the following:

$$P(t)_{RSB} = \sum_{n=0}^{\infty} \rho_{nn} \sin^2 \Omega_{n,n-1} t, \tag{2.16}$$

$$P(t)_{BSB} = \sum_{n=0}^{\infty} \rho_{nn} \sin^2 \Omega_{n,n+1} t \tag{2.17}$$

where $\rho_{nn} = \langle n| \rho |n\rangle$ are the Fock-state populations of the motional state and

$$\Omega_{n,n-1} = \eta\Omega\sqrt{n}; \Omega_{n,n+1} = \eta\Omega\sqrt{n+1} \tag{2.18}$$

where η is the Lamb-Dicke parameter. Under the assumption the motional state is in a thermal state, the Fock-state populations can be re-written as proportional to the partition function $\rho_{nn} = \frac{1}{\mathcal{Z}}\alpha^n$, where $\alpha = e^{-\omega/k_b T}$ and $\mathcal{Z} = \sum_n \alpha^n = 1/(1-\alpha)$. Rewriting the summations for the RSB and BSB and gives us a measurement to determine $\bar{n}$

$$\bar{n} = \frac{P(t)_{RSB}}{P(t)_{BSB} - P(t)_{RSB}} \tag{2.19}$$

at any arbitrary time t. By comparing the contrast of RSB and BSB, we can determine the average phonon number. An example of this measurement in shown in Figure 2.7.

2.3 Quantum Gates

For the $^{171}Yb^+$ ion, the hyperfine transition between the $\left|F = 0, m_f = 0\right\rangle$ and $\left|F = 1, m_f = 0\right\rangle$ in the $^2S_{1/2}$ manifold is well characterized at $\omega_0 = 2\pi \times 12.642812118526$

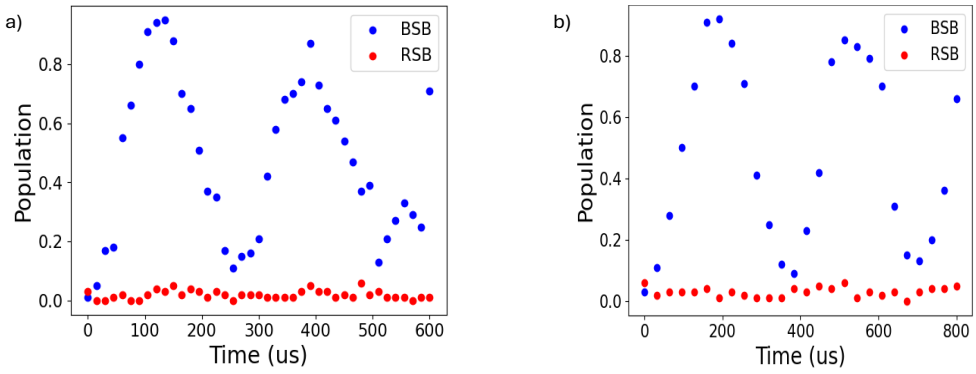

FIGURE 2.7: **Sideband cooling measurements of the two lowest frequency modes for the center ion.** a) Red (RSB) and Blue (BSB) sideband transitions for the zig-zag mode. Measured $\bar{n} = 0.0424$ b) RSB and BSB for the second lowest frequency mode for the center ion. Measured $\bar{n} = 0.0772$

GHz + $310.8(B^2)$ Hz. We can define the qubit state to be encoded into this hyperfine structure where $|0\rangle = \left|F = 0, m_f = 0\right\rangle$ and $|1\rangle = \left|F = 1, m_f = 0\right\rangle$. Now that we know the frequency between the qubit states, there are two predominant methods to conduct gates between these levels — resonant microwave fields and stimulated Raman transitions.

2.3.1 Microwave Gates

Due to the natural frequency of the hyperfine level, a microwave frequency source is the most natural way to drive the transition between the defined qubit states. We can represent the microwave electric field as $\mathbf{E}$, with a respective frequency ω and phase ϕ. The atomic Hamiltonian $H^{(a)}$ and the interaction Hamiltonian due to the magnetic field H_I can be written as

$$H^{(a)} = \hbar\omega_{10} |1\rangle\langle 1| \tag{2.20}$$

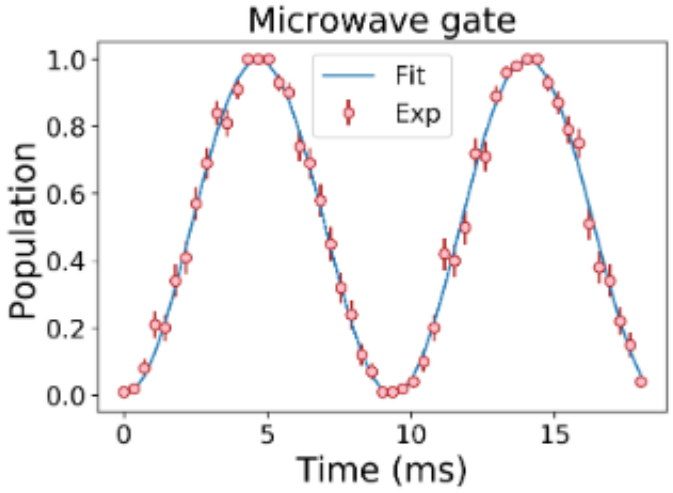

FIGURE 2.8: **Example microwave driven transition.** The red dots represent the experimental data with error bars. The blue line represents an ideal Rabi flop. *Data collected 10-11-2023.*

$$H_I = \hbar\Omega[e^{-i(\omega t+\phi)} |1\rangle\langle 0| + h.c.] \tag{2.21}$$

where Ω is the effective Rabi frequency due to the magnetic field. By defining a rotating frame using the driving magnetic frequency $H = \hbar\omega |1\rangle\langle 1|$, and transforming our interaction Hamiltonian via

$$\tilde{H}_I = UHU^\dagger + i\hbar\frac{\partial U}{\partial t}U^\dagger \tag{2.22}$$

where $\tilde{H}_I$ is now the interaction Hamiltonian in the rotating frame and $U = e^{iH_D t/\hbar}$ we obtain the following rewritten Hamiltonian

$$\begin{aligned}\tilde{H} &= H^{(a)} - H_D + \tilde{H}_I \\ &= \hbar(\omega_{10} - \omega) |1\rangle\langle 1| + \hbar\Omega[e^{-i\phi} |1\rangle\langle 0| + h.c.]\end{aligned} \tag{2.23}$$

Thus, we see if we identify the exact hyperfine frequency, we can drive the microwave transition using $\omega = \omega_0$. This can be seen in the Rabi flop shown in Figure 2.8.

In practice, to generate the hyperfine microwave frequency, we use an ultra-low phase noise Syntonix quartz oscillator to produce a 12.6 GHz source. The 12.6 GHz is mixed with a signal from a direct digital synthesizer (DDS) that can arbitrarily produce a RF signal up to a few hundred MHz. The resultant mixed signal is amplified and sent to a waveguide gain horn. By scanning the DDS signal's frequency to identify the additional 42.8 (...) MHz needed to drive the transition; the horn's produced wave packet directed at the ion's location and can drive a quantum gate. From the measured microwave frequency at 12.642820(0) GHz, we can calculate the applied magnetic field at ≈ 5.037 Gauss.

There are two additional Zeeman levels in the ${}^2S_{1/2}$ manifold of ${}^{171}Yb^+$ we can address through the same technique. We scan the DDS to find the ${}^2S_{1/2}\left|F=0,m_f=0\right\rangle \rightarrow {}^2S_{1/2}\left|F=0,m_f=-1\right\rangle$ at 35.757436(1) MHz and ${}^2S_{1/2}\left|F=0,m_f=0\right\rangle \rightarrow {}^2S_{1/2}\left|F=0,m_f=1\right\rangle$ at 49.873982(5) MHz. From these measurements, we can identify the Zeeman splitting ν_{Zeeman} is 7.053967 MHz, giving us an inferred applied magnetic field at $B \approx 5.04$ Gauss. The calculated strength of the magnetic field agrees with the aforementioned carrier frequency.

2.3.2 Raman Transitions

Consider a three-level atomic system as shown in Figure 2.9 confined in a harmonic potential interacting with two laser beams each with respective frequency ω_i and electric field $\vec{E}_i$, where $\vec{E}_i = E_0^{(i)}\hat{\epsilon}\cos\left(\omega_i t - \vec{k}_i\cdot\vec{x}+\phi_i\right)$. The Hamiltonian for the atomic system, $H^{(a)}$, and its motional state, H^m, can be written as

$$H^{(a)} = \hbar\omega_{10}\left|1\right\rangle\left\langle 1\right| + \hbar\omega_{20}\left|2\right\rangle\left\langle 2\right|, \tag{2.24}$$

and

$$H^{(m)} = \hbar\nu(a^\dagger a + \frac{1}{2}) \tag{2.25}$$

where the energy level of $|0\rangle$ has been set to zero. The phonon creation and annihilation operators have been represented above by $a^\dagger$ and a respectively. For the interaction Hamiltonian, the electric field interacts with the atomic dipole, given by $\vec{r} = \hat{r}(d_{if}\left|i\right\rangle\left\langle f\right| + h.c.)$

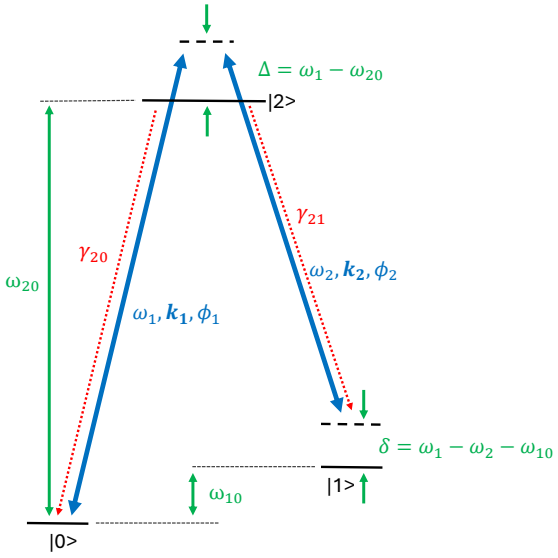

FIGURE 2.9: **Depiction of typical λ system for a Raman transition.** The two Raman lasers are shown with the blue lines, with respective frequency ω, k-vector **k** phase ϕ. The frequency detunings for each of the virtual states are shown as Δ and δ.

where i and f represent the initial and final states of any given transition. Consequently, the interaction Hamiltonian can be written as $H_I = -q\vec{E}\cdot\vec{r}$. For both beams, we can write this out explicitly as

$$\begin{aligned} H_I = & -qE_0^{(1)}\hat{\epsilon_1}\cos\Big(\omega_1 t - \vec{k}_1\vec{x} + \phi_1\Big)\hat{r}(d_{02}\,|0\rangle\langle 2| + h.c.) \\ & -qE_0^{(2)}\hat{\epsilon_2}\cos\Big(\omega_2 t - \vec{k}_2\vec{x} + \phi_2\Big)\hat{r}(d_{12}\,|1\rangle\langle 2| + h.c.) \end{aligned} \tag{2.26}$$

Defining the Rabi frequency for each beam as $\Omega_1 = -qE_0^{(1)}\hat{\epsilon_1}\cdot\hat{r}d_{02}/\hbar$ and $\Omega_2 = -qE_0^{(2)}\hat{\epsilon_2}\cdot\hat{r}d_{12}/\hbar$ gives us

$$\begin{aligned} H_I = & (\hbar\Omega_1\,|0\rangle\langle 2| + \hbar\Omega_1^*\,|2\rangle\langle 0|)\cos\Big(\omega_1 t - \vec{k}_1\vec{x} + \phi_1\Big) \\ & (\hbar\Omega_2\,|1\rangle\langle 2| + \hbar\Omega_2^*\,|2\rangle\langle 1|)\cos\Big(\omega_2 t - \vec{k}_2\vec{x} + \phi_2\Big) \end{aligned} \tag{2.27}$$

At this point, we perform a unitary transformation to move the Hamiltonian into the rotating frame characterized by $U = \exp\{(-iH_D t/\hbar)\}$ where $H_D = H^{(a)} + H^{(m)}$. In

Table 2.1: Relevant Raman frequency scales to drive transitions for $^{171}Yb^{+}$. All frequencies are angular and are multiplied by 2π.

Parameter	Notation	Angular Frequency ($\times 2\pi$)
355nm pulsed laser beam	ω_1, ω_2	844 THz
Photon detuning from $^2P_{1/2}$	Δ	33 THz
Hyperfine Splitting	ω_{10}	12.64 GHz
Rabi Frequency	Ω_1, Ω_2	3.9 GHz
Spontaneous emission rate	γ	19.64 MHz
Trap Frequency	ν	2 MHz

addition, we consider the relative frequencies of each aspect in our Raman transition setup, shown in Table 2.1.

Using Eq 2.22, the interaction Hamiltonian in the rotating frame is

$$\tilde{H_I} = -h\Delta \left|2\right\rangle\left\langle 2\right| + \frac{\hbar\Omega_1}{2}[\left|2\right\rangle\left\langle 0\right| e^{i\vec{k}\cdot r(\vec{t})-\phi_1} + h.c.] + \frac{\hbar\Omega_2}{2}[\left|2\right\rangle\left\langle 1\right| e^{i\vec{k}\cdot r(\vec{t})-\phi_2+\delta\cdot t} + h.c.] \quad (2.28)$$

and given that $\Delta \gg \omega_{10} \gg \Omega_{1,2} \gg \gamma > \nu$, we can adiabatically eliminate the excited state $\left|2\right\rangle$, resulting in the final equation for the Raman transition between states $\left|0\right\rangle$ and $\left|1\right\rangle$ as

$$\tilde{H_I} = \hbar\frac{\Omega_1\Omega_2}{4\Delta} e^{-i[\Delta\vec{k}\cdot\vec{r}-\delta t-\Delta\phi]} \left|0\right\rangle\left\langle 1\right| + h.c. \quad (2.29)$$

where $\Delta\vec{k} \equiv \vec{k_1} - \vec{k_2}$ and $\Delta\Phi \equiv \phi_1 - \phi_2$.

2.3.3 Single Qubit Gates and Spin Coherent Kicks

Starting from the phase-sensitive Raman transition Hamiltonian and assuming that $\Delta\vec{k}$ is only parallel to the motional modes in one direction, we can simplify $\Delta\vec{k}\cdot\vec{r}$ to Δkx and rewrite Equation 2.29 as

$$\begin{aligned} \tilde{H_I} = \hbar\frac{\Omega_1\Omega_2}{4\Delta} e^{i[\Delta kx-\delta t-\Delta\phi]} \left|1\right\rangle\left\langle 0\right| + h.c. \\ \hbar\frac{\Omega_{eff}(x)}{2} e^{i[\Delta kx-\delta t-\Delta\phi]}\hat{\sigma}_+ + h.c. \end{aligned} \quad (2.30)$$

where in the last line, I have defined the effective Rabi frequency as $\Omega_{eff}(x) = \Omega_1\Omega_2/2$ and the raising operator $\sigma_+ = |1\rangle\langle 0|$. Taylor expanding this expression to first order around $x = x_0$, and assuming $x_0 = 0$, we obtain without losing generality:

$$\tilde{H_I} \approx \hbar(\frac{\Omega_{eff}(x_0=0)}{2} + \frac{\Omega'_{eff}(x_0=0)}{2}x + i\Delta k x\frac{\Omega_{eff}(x_0=0)}{2} + ...)e^{i(-\delta t-\Delta\phi)}\hat{\sigma}_+ + h.c. \tag{2.31}$$

The ion's position, x, can be quantized as

$$x = \sqrt{\frac{1}{2mw}}(\hat{a}e^{-i\omega t} + \hat{a^\dagger}e^{i\omega t}) \tag{2.32}$$

where ω is the ion mode's motional frequency. Considering the ion position in terms of the Lamb-Dicke parameter, where $\eta \equiv \Delta k\sqrt{1/2m\omega}$, then $x = \frac{\eta}{\Delta k}(\hat{a}e^{-i\omega t} + \hat{a}^\dagger e^{i\omega t})$. The Lamb-Dicke parameter measures the interaction between the spin and the motional states. We assume the interaction is sufficiently small such that any interaction that changes the motional quantum number by more than one are suppressed, further justifying the first order Taylor expansion in Equation 2.31.

When $\delta = 0$, the Raman transition gives us exactly the qubit hyperfine splitting, ω_{10} in Figure 2.9. We typically refer to this as the carrier transition, written as

$$H_{carrier} = \hbar\frac{\Omega(0)}{2}e^{-i\Delta\phi}\hat{\sigma}_+ + h.c. \tag{2.33}$$

Here, only the zeroth-order term is reserved, and higher order terms involving the motion are neglected. This treatment is accurate, even if the Lamb-Dicke parameter is not zero, as long as the δ used to resonantly drive the carrier transition is far-detuned from the motional sideband transitions (in practice $\approx 2\pi \times 1.6 - 2MHz$ detuned). This interaction will be the foundation of the single qubit gates we describe in Chapter 5 with the spin phase $\Delta\phi$ setting the angle of rotation for the gate.

When $\delta = \omega$, the carrier transition is neglected under the rotating wave approximation (RWA), and our treatment focuses on the second and third term in Equation 2.31. The remaining component represents our blue sideband transition (BSB) and can be written:

$$H_{BSB} = (\frac{\Omega^{'}(x_0 = 0)}{2}\frac{\eta}{\Delta k} + i\eta\frac{\Omega(x_0 = 0)}{2})e^{-i\Delta\phi}\hat{a}^{\dagger}\hat{\sigma}_{+} + h.c. \tag{2.34}$$

Similarly, for the red sideband transition, at $\delta = -\omega$, we get

$$H_{RSB} = (\frac{\Omega^{'}(x_0 = 0)}{2}\frac{\eta}{\Delta k} + i\eta\frac{\Omega(x_0 = 0)}{2})e^{-i\Delta\phi}\hat{a}\hat{\sigma}_{+} + h.c. \tag{2.35}$$

Applying both the RSB and BSB transitions together, we obtain an expression for a spin-dependent kick (SDK)

$$\begin{aligned} H_{SDK} &= H_{BSB} + H_{RSB} \\ &= |A|(e^{-i(\Delta\phi-\gamma)}\hat{\sigma}_{+} + h.c.)(\hat{a} + \hat{a}^{\dagger}) \end{aligned} \tag{2.36}$$

where I have defined A to represent the coefficient $(\frac{\Omega^{'}(x_0=0)}{2}\frac{\eta}{\Delta k} + i\eta\frac{\Omega(x_0=0)}{2})$ and $\gamma = Arg(A)$. In this expression, the spin phase of the operation, denoted ϕ_s is obtained from $\phi_s = \Delta\phi - \gamma$. We will exploit this phase in Chapter5 when examining different SDK angles.

The more general spin-state-dependent coherent displacement Hamiltonian can be written as

$$H_{SDK} = i\Omega(\sigma_{+}e^{i\phi_s} - \sigma_{-}e^{-i\phi_s})(a^{\dagger}e^{i\phi_m} + ae^{-i\phi_m}) \tag{2.37}$$

where $\phi_s = (\phi_B + \phi_R)/2$ and $\phi_m = (\phi_B - \phi_R)/2$ [Jia et al., 2022]. We have a similar spin phase in this Hamiltonian, but now also have a motion phase ϕ_m.

3. Experiment Infrastructure

The experimental system utilized in the quantum simulations described in Chapter 5 consists of a room temperature ultra-high vacuum chamber with a Sandia Phoenix surface trap [Revelle, 2020]. Although I did not create this system, I participated in or personally conducted all the experiments written in this thesis. Furthermore, I created a very similar system which did not have the requisite Raman lasers for gate operations, so it was abandoned. The latter system, referred to as the EPICS system, was a new system meant to demonstrate improved photon collection for state detection. The hardware revolved around an optical cavity installed in ultra high vacuum, with its own independent vacuum chamber. The efforts to demonstrate this cavity are shown in Chapter 4.

3.1 Experiment Hardware

Inside our vacuum chamber, we use the Phoenix trap attached to a ceramic pin grid array (CPGA) which is connected to a Rogers 6002 printed circuit board (PCB). The circuit board and trap materials are specifically chosen to minimize out-gassing rates. The trap potential is formed from a combination of DC and RF voltages generated through independent direct digital synthesis (DDS) channels which are then routed through the PCB to the respective CPGA pins. To minimize noise, the DC channels are passed through a low-pass filter box with a 2 kHz cut-off frequency. For the RF signal, it is first amplified by a low-noise 30 dB gain amplifier then connected to a helical resonator. The resonator, described by Siverns et al., 2012, has a quality factor that is a function of its inductance L, capacitance C, and resistance R

$$Q = \frac{1}{R}\sqrt{\frac{L}{C}}. \tag{3.1}$$

In principle, the peak voltage of the resonant circuit with input power P is given by

$$V_{RF} \approx (\frac{L}{C})^{1/4}\sqrt{2PQ}. \tag{3.2}$$

We can measure the trap voltage directly via a capacitive pick-off integrated into the PCB design. Inside the helical resonator, there is an inner coil that is directly connected to the amplified RF signal. The inner coil inductively couples to the main solenoid, decoupling the amplifier's output resistance (usually at 50 Ω) from the resonant circuit. Impedance matching between the inner coil and the main resonator coil is accomplished in practice by adjusting the coil overlap until the power transferred to the resonator is maximized. The quality factor for this experiment's resonator was approximately 150.

3.2 Ultra-high Vacuum Environment

In order to trap an atomic ion and minimize collisions with background gas molecules, we need an ultra-high vacuum (UHV) environment with an operating pressure between 10^{-11} to 10^{-12} Torr. We use a Kimball Physics octagon chamber with seven side viewports, one large front viewport, and one small back viewport. The ion trap, the ablation target filled with ytterbium and the electronic feedthroughs for RF and DC fields are all mounted in the main octagon chamber. A Titanium sublimation pump (Ti-sub), all metal valve, and an ion gauge port are also attached to the chamber, each of which serves an important purpose during the chamber bake-out. After the bake-out, a connected ion pump is running continuously to maintain the low pressure vacuum. Lastly, a ring of permanent magnets are also mounted to the chamber's back flange.

3.2.1 Assembly and Baking

To achieve the low pressure needed to run a trapped ion experiment, we follow a very strict cleanliness protocol. Before assembly, every part, with the exception of the Phoenix trap, is cleaned with acetone and isopropanol in an ultra-sonic bath. After each bath, each part is blown dry with nitrogen to remove any contaminants dissolved within the solvent. They are then 'pre-baked' for approximately one day at 200°C to ensure any residual water vapor has evaporated and to form a thin oxide layer on the surface of the metal parts. The chamber is then opened and assembled within a Class 4 cleanroom. In the cleanroom, while the chamber is open, the all metal valve is connected to a steady supply of nitrogen as an

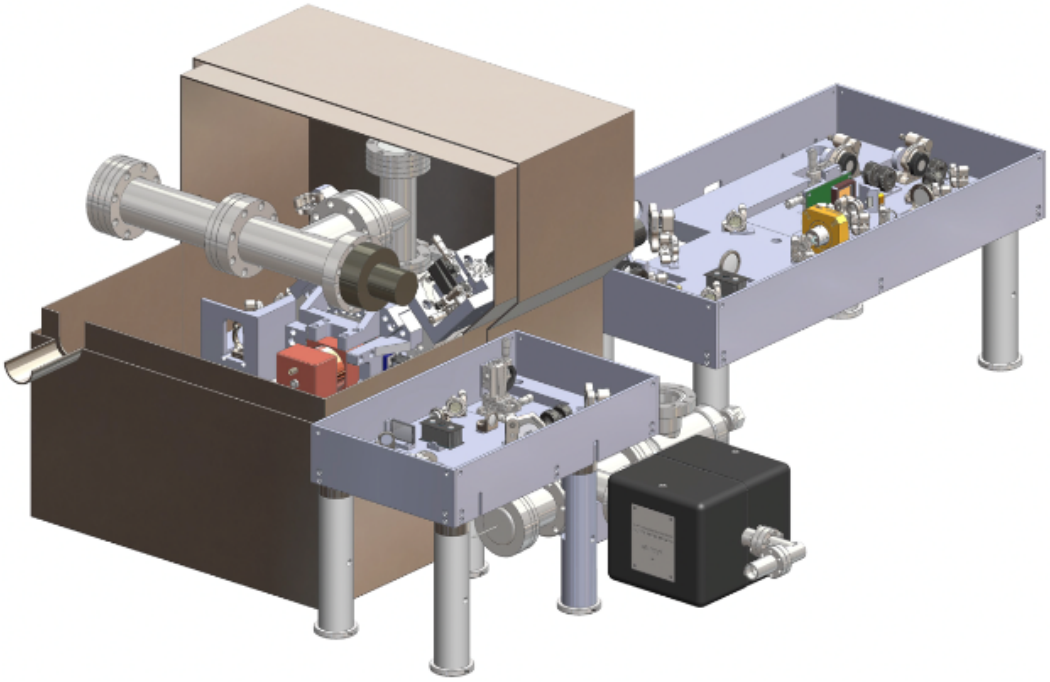

FIGURE 3.1: **Solidworks CAD drawing of Red Chamber inside μ-metal shield with attached beam $^{171}Yb^{+}$ delivery system.** Global and individual Raman delivery plates are also shown

additional precaution to prevent contamination inside the chamber.

Simply having a very clean environment is not sufficient to achieve UHV conditions. We use a sequence of pumps to reach the desired pressure. The chamber is first exposed to a roughing pump to bring the chamber from atmospheric pressure to e^{-3} Torr. Then a turbomolecular pump (TMP) is turned on to reach e^{-7} Torr. The TMP is turned on under an elevated temperature to remove contaminants, including but not limited to hydrocarbons and water vapor, which can adhere to surfaces within the chamber interior. The high temperature increases these contaminants' vapor pressure, allowing them to evaporate and then be pumped away. Once the TMP has bottomed out the pressure, the last stage of pumping is the ion pump allowing us to reach below e^{-11} Torr.

Once the trap is installed, the entire chamber is placed into a large oven with programmable temperature control. We then follow the outlined pump procedure.

1) The all metal valve is attached to the turbo pump with an integrated leak detector and pumped until the gauge reads 2e-8 mbar. At this time, we scan all the connection joints with a small amount of helium to check for leaks.

2) The chamber is covered in aluminum foil to address any temperature gradients within the oven.

3) The temperature is ramped to 120°C at a rate of 9°C/hr

4) Once the chamber reaches 120°C, the Ti-Sub is degassed (42 A for 2 minutes). The ion-pump is also degassed to remove any contaminants for about 2 hrs. The ion gauge is turned on, degassed and used to monitor the pressure from this point. We also degas the small ion pump at this point, but leave it off until later during the bake-out.

5) We close the all metal valve which had been connected to the turbo pump and open the valve to engage the large ion pump.

6) The temperature is ramped to 180°C at a slower rate of 5.4°C/hr.

7) We keep the chamber at this temperature for approximately 72 hrs. The RGA is monitored during this time and described in detail in Sun, 2024

By following the above procedure, we minimize the risk of cracking the chamber windows (occurs at ramp speeds above 10°C/hr), damaging the window coatings ($>$ 180°C), or causing purple plague in the surface trap (@200°C for long durations).

3.3 Laser Control

In order to control and interact with our trapped ion, we primarily use laser light. These lasers need to be precisely locked to the atomic transition frequencies with a well-defined spatial mode and power output. The five relevant wavelengths for $^{171}Yb^{+}$ are 355 nm, 369.5 nm, 935 nm, 399 nm, and 1064 nm. The last three wavelengths do not need real-time control so their set-up is relatively straightforward. The 935 nm requires a 3.1 GHz EOM fiber EOM and a wavemeter lock to repump the D sub-level described in Chapter 2. The 399 nm just needs a mechanical shutter, sufficient power to photoionize the neutral ytterbium and a wavemeter monitor to tune to the relevant isotope.

3.3.1 Ion Loading

During ion loading, the 1064 nm nanosecond pulsed ablation laser, aligned to the ablation target shown in Figure 3.3, is switched on to create a neutral flux of Yb atoms. The mechanical shutter blocking 399 nm is removed, allowing for both 399 nm and 355 nm to overlap inside the chamber. The neutral flux and the aforementioned lasers intersect above the trapping region to photo-ionize the neutral Yb flux creating $^{171}Yb^{+}$ ions.

3.3.2 370 nm

Our 370 nm plates are used for Doppler cooling, state initialization and EIT cooling. The plate layout, as shown in 3.2, uses ≈1.5 mW of 370 nm light and through a series of AOMs splits this light into upstream fiber ports which are then connected to the fiber launches shown in 3.3. Each AOM's RF power is connected to an electrical minicircuit switch-linked to a TTL for control. All of the TTLs are controlled in real-time during circuit operation via the RFSoC firmware.

3.3.3 355 nm

All of our qubit operations are controlled by a coherent Paladin 355 nm laser. This turn-key laser is propagated onto two water-cooled plates at $16°C$ that control a single 'global' beam and two 'individual' beams. The plate layout is described in detail in [Zhang, 2021].

3.3.4 Laser AOM Control and Locking

The RFSoC firmware, provided by Sandia National Laboratories' QSCOUT project, is a sophisticated DDS we use to control the amplitude, phase, and frequency of each beam. Each channel supports a two-tone output, which is naturally convenient for running our spin-coherent kicks. In addition, it supports complex modulations of each tone, allowing for arbitrary amplitude and phase pulse definitions.

One key feature of the RFSoC is a built-in Raman repetition rate stabilizer. The 32nd harmonic from the 355 nm laser is measured from a photodiode. This signal is mixed with a 3.7 GHz microwave source and read into an ADC of the RFSoC. The measured ADC

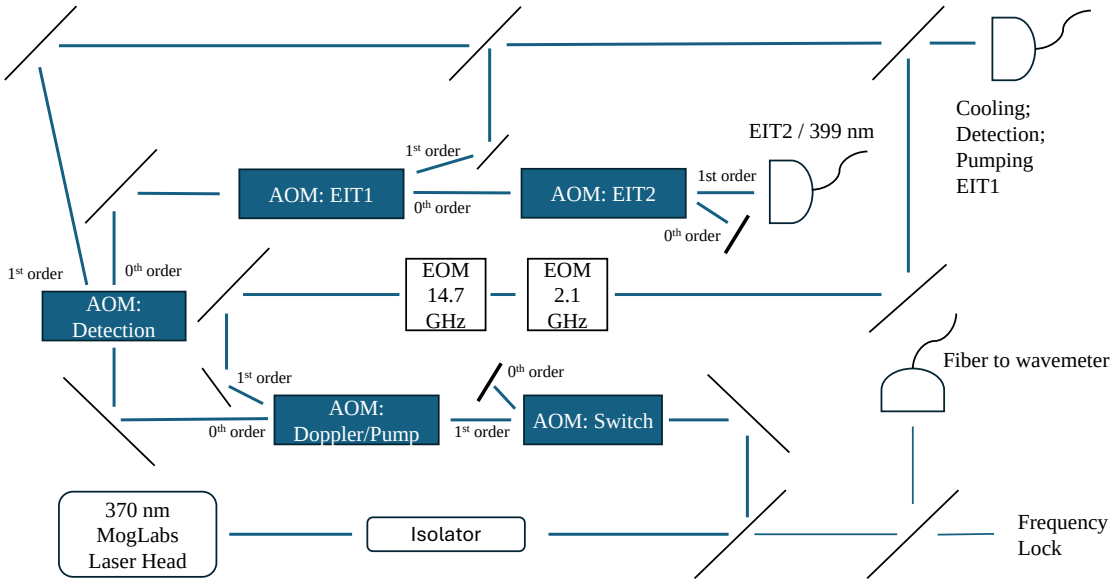

FIGURE 3.2: **Box Layout of our 370 nm plate.** Two fiber ports are linked to the chamber (cooling, pumping, detectiong, EIT1, and EIT2). The last fiber port is used in a monitor the frequency. The frequency is set to be 15 MHz red-detuned from the cycling transition frequency.

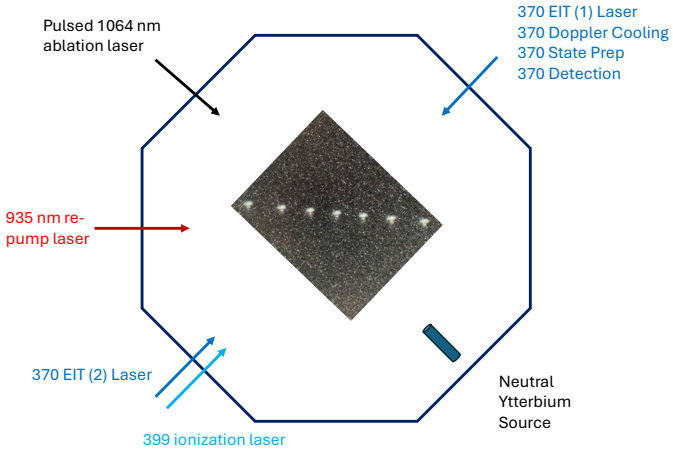

FIGURE 3.3: **Laser configuration for trapping Ytterbium around the steel octagon.** 399, 370 and 935 nm laser configuration are shown relative to our Kimball Octagon chamber and the center ion chain. An example of 7 ions is shown in the center taken from our imaging system.

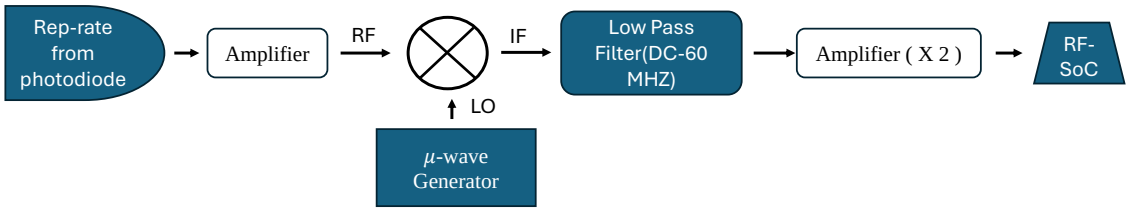

FIGURE 3.4: Raman repetition rate stabilization up to the RFSoC. The μwave source is at 3.7 GHz. The measured rep-rate from the photodiode is the 32nd harmonic of the 355 nm laser.

input is mixed with a setpoint frequency. The beatnote, mixed with a feedback signal from a built-in PID, serves as an error signal to stabilize the Raman control. Of note, the Raman laser is not itself stabilized, but added onto the RF output. The design of this lock is shown in Figure 3.4.

3.4 System Characterization

3.4.1 Micromotion Compensation

To characterize the micromotion shown in Equation 2.7, we use a time-correlated single photon counting (TCSPC) PicoHarp device to analyze counts registered from one of the photomultiplier tube (PMT) channels and a pickoff from the trap RF signal. If there is a strong correlation in these temporally correlated measurements, this indicates the ion is oscillating at the same frequency as the trap RF. By adjusting the DC null, we can minimize this correlation, as shown in Figure 3.5.

For our particular experiment, the Doppler cooling light predominantly lies in the x-y plane of the trap. As this method measures the photon emitted during Doppler scattering,

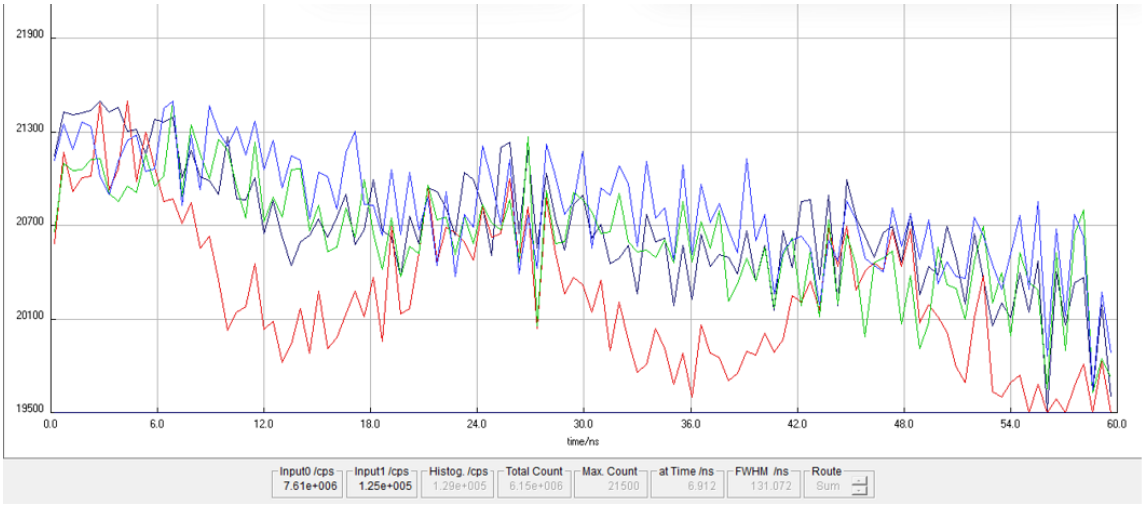

FIGURE 3.5: **PicoHarp time-correlated measurement of micromotion on the center ion.** By adjusting the DC null along the y-axis, we can minimize the measured oscillations occurring at the RF frequency. As the DC null is adjusted the micromotion is minimized, evidenced by the minimization of the oscillation frequency from the Red curve to the Blue curve.

it is most sensitive to ion micromotion in the x-y plane. Since the x-plane is the axial direction of our trap, we primarily use this method to counteract micromotion in the y-direction. Adjusting the ion's y-position results in significant mitigation of the temporally correlated measurements, as evidenced by the blue curve in Figure 3.5.

3.4.2 Crosstalk

To implement the Raman transition, we use an elliptical global beam and a roughly circular individual beam to drive the qubit. The measured global elliptical waist is 94.75 μm $\times$ 8.89μm and the circular beam is 1.45μm $\times$ 1.54 μm. In addition, in order to drive any two-qubit gate operations, we have a second individual beam with approximately the same dimensions but have it pointed at a different ion. When driving any single qubit operation, each respective individual beam should only drive the transition of one ion. We can test this by creating a five-ion chain, with each ion spatially separated from each other by about 5 μm. By monitoring the qubit state of all five ions, we can quantify the 'crosstalk' between the target ion and its neighbors. These results are shown in Table 3.1. The 1-2% crosstalk seen in the Rabi frequency of some of the neighboring ions can be described by the

Table 3.1: Ratio of measured Rabi frequency between target ion and neighbors in a 5-ion chain. The Raman beam is on ion 3 and the second individual Raman is on ion 4.

Raman Individual Beam	Ion 1	Ion 2	Ion 3	Ion 4	Ion 5
Ind 1	0.0122	0.0117	*target*	0.007	0.0175
Ind 2	0.00981	0.0219	0.00981	*target*	0.00455

imperfect Gaussian shape of the individual Raman, resulting in a portion of the scattered light driving the transition.

3.4.3 Coherence Time

The ability to conduct quantum gates is directly correlated to the qubit's coherence time. Often referred to as the T_2 time, this time characterizes how long a qubit remains coherent before decoherent effects become predominant and the ion quantum state is now mixed. It serves as the fundamental time threshold for a quantum simulation where reliable quantum gates can still be implemented.

Our coherence times were measured via the Ramsey method. The technique uses two $\pi/2$ pulses with a long wait time τ separating the pulses. By varying the wait time τ between the pulses, the ion qubit experiences any external perturbations which can decohere the quantum state. As the ion state continually evolves during this wait time, there is an additional phase which may make the second $\pi/2$ out of phase. Consequently, we scan the phase of the second pulse and analyze the fringe contrast to best understand the system's T_2 time. The results of these measurements are shown in Figure 3.6.

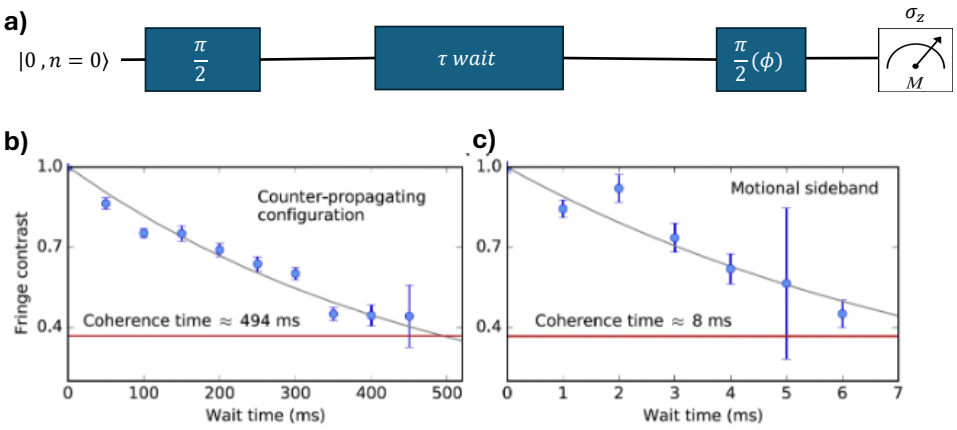

FIGURE 3.6: **Ramsey method for characterizing T2 time.** a) Outline of Ramsey circuit used to characterize the decoherence. b) Fringe contrast measured for counter-propagating Raman transition c) Fringe contrast measured for blue sideband transition.

4. Cavity Integration with Surface Traps

Cavity quantum electrodynamics (CQED) is a field dedicated to understanding the interaction of optical cavities with atoms. A cavity QED system exchanges energy between a cavity mode and an atomic array giving rise to quantum mechanical behavior that is not only relevant for quantum computation, but potentially very beneficial. In this chapter, I will discuss an important application of such a system, efficient photon collection.

4.1 Photon Emission

An atomic system can emit a photon through two processes, stimulated and spontaneous emission. In the former, an incoming photon induces an atomic electron in an excited state to decay to the ground state, while the latter has the excited state spontaneously decay to the ground state. To understand the emission rate, we start with a quantized radiation field, written as

$$\mathbf{E} = \sum_{\mathbf{k}} \mathbf{C}_{\mathbf{k}} \hat{\epsilon}_{\mathbf{k}} (a_{\mathbf{k}} + a_{\mathbf{k}}^{\dagger}) \tag{4.1}$$

with field strength $\mathbf{C}_{\mathbf{k}} = \sqrt{\frac{\hbar\omega_{\mathbf{k}}}{2\epsilon_0 V}}$. Here, V is the volume of the cavity mode and ω_c is the photon's angular frequency. The general Hamiltonian of a single-electron atom interacting with this quantized field, commonly referred to as the Jaynes-Cummings Hamiltonian [Scully and Zubairy, 1997], takes the form:

$$H = \sum_{k} \hbar\omega_k a_k^{\dagger} a_k + \frac{1}{2}\hbar\omega_a \sigma_z + H_{Int} \tag{4.2}$$

The Jaynes-Cummings Hamiltonian's first two terms, respectively, describe the radiation field's energy and the atom's energy levels in the absence of any interaction. The interaction term, which describes the coupling between the quantized field and the atom, has a coupling strength of g_k^{eg} written as [**Scully**]

$$g_k^{eg} = \frac{\mu_{eg}}{\hbar}\sqrt{\frac{\hbar\omega_c}{2\epsilon_0 V}}. \tag{4.3}$$

The coupling strength is proportional to the electric-dipole transition matrix element between the excited and ground state, $\mu_{eg} = e|\langle e|\vec{r}\,|g\rangle|$. The dipole moment quantifies the separation between the system's excited and ground states' charge distributions. To interact with the atom, the quantized electric field needs a component along this direction to drive a transition between the quantum states.

The interaction Hamiltonian is often written under the rotating-wave approximation (RWA), where higher-frequency terms that oscillate above $\omega_a + \omega_k$ are neglected as they break energy conservation.

$$H_{Int} = \hbar \sum_k g_k(\sigma_+ a_k + a_k^\dagger \sigma_-) \tag{4.4}$$

The interaction Hamiltonian describes a very intuitive picture between the atomic transition ladder operators, σ_- and σ_+, and the photon creation and annihilation operators, $a^\dagger$ and a respectively. In one scenario, $\sigma_- a^\dagger$, when the atomic state relaxes from the excited state to the ground state, a corresponding photon is created. Alternatively, in the term $\sigma_+ a$, when a photon is annihilated or absorbed, the atomic state transitions from the ground state to the excited state. These vacuum Rabi oscillations occur at a rate $2g$ for a resonant system.

The interaction picture for Eq 4.4, using the first two terms in Eq 4.2 as our rotating frame, H_0, is written as

$$H' = e^{iH_0 t/\hbar} H_{Int} e^{-iH_0 t/\hbar} = \hbar \sum_k (g_k \sigma_+ a_k e^{i(\omega-\nu)t} + h.c.). \tag{4.5}$$

Under the spontaneous emission condition, we know that at time $t = 0$, the atom is in the excited state $|e\rangle$ and the vacuum modes are in state $|0\rangle$. Thus, we can start with a state vector

$$|\Psi\rangle = c_e(t)|e,0> + \sum_k c_{g,k}(t)\,|g,1_k\rangle \tag{4.6}$$

under the condition $c_e(t=0) = 1$ and $c_{g,k}(t=0) = 0$. Solving the Schrödinger equation

with this initial condition, we find the exact expression

$$\frac{d}{dt}c_e(t) = -\sum_k |g_k|^2 e^{i(\omega_a-\omega_k)t|}\int_0^t c_e(t')e^{-i(w_a-w_k)(t'-t)}dt' \tag{4.7}$$

In the continuum limit, where the quantization volume tends to infinity, we can make the following substitution $\sum_k \rightarrow \int d^3kD(k)$ where $D(k)$ is the density of states in k-space. Thus, we see the atomic population rate of change is directly proportional to the vacuum mode's density of states which will become relevant when we consider introducing a dielectric. Since $\mathbf{k} = (2\pi n_1/L, 2\pi n_2/L, 2\pi n_3/L)$, there is one state in volume and $D(k) = (L/2\pi)^3 = V/(2\pi)^3$. Using $k = \omega_k/c$, and substituting Eq 4.3, Eq 4.7 becomes in spherical coordinates

$$\frac{d}{dt}c_e(t) = -2\frac{\mu_{eg}^2}{(2\pi)^3 2\hbar\epsilon_0 c^3}\int_0^{2\pi} d\phi \int_0^{\pi} d\theta \cos^2\theta \sin\theta \int_0^{\infty} d\omega_k \omega_k^3 \int_0^t c_e(t')e^{-i(w_a-w_k)(t'-t)}dt' \tag{4.8}$$

where θ is the angle between the dipole moment and the polarization vector. There is an additional pre-factor of 2 in the integration due to the two allowed polarization states.

Looking just at the last time term in Eq. 4.8, this exponential oscillates with frequency ω_a which we assume is much faster than the rate of change for the excited state, Γ. Referred to as the Weisskopf-Wigner approximation, $c_e(t)$ can be pulled out of the integrand and the last term evaluates to $2\pi\delta(t-t')$. Evaluating the rest of the integral, we obtain the result of Wigner-Weisskopf theory, also referred to as the Einstein A coefficient

$$\frac{d}{dt}c_e(t) = -\frac{\Gamma}{2}c_e(t)$$

where

$$\Gamma = \frac{\omega_c^3 d_{eg}^2}{3\pi\epsilon_0\hbar c^3}. \tag{4.9}$$

The final result indicates that the spontaneous emission rate is a fundamental property of the atom and from this point the rate will be considered constant. Furthermore, it is

important to note that spontaneous emission in free space can emit in a random direction over a full 4π solid angle due to the vacuum mode's symmetry. However, we see in Eq. 4.7, by decreasing the interacting field's mode volume, we increase the vacuum Rabi rate Eq. 4.3 and the rate of change for the excited state population. An optical cavity addresses both of these limitations, decreasing the effective mode volume and breaking the symmetry by altering the density of states such that the photon emits preferentially into the cavity mode.

4.2 Cavity Theory and Density of States

An optical Fabry-Perot cavity is made up of two highly reflective mirrors that can support a standing wave at evenly spaced frequencies. This means an electric field acquires a multiple of a 2π phase shift after one round trip within the cavity. The optical resonator can be stable if and only if the confinement condition is satisfied

$$0 < g_1 g_2 < 1 \tag{4.10}$$

where $g_n = 1 + \frac{d}{R_n}$. Here, d is the cavity length and R_n is the Radius of Curvature (ROC) for each respective mirror. This condition can be summarized as an optical cavity requires an integer number of half wavelengths to fit inside the cavity, or $l = n\lambda/2$ for a cavity of length l using wavelength λ. As we will be working exclusively with semispherical resonators, $R_2 \to \infty$ and $g_2 \to 1$, our stability equation simplifies to $0 \leqslant g_1 \leqslant 1$.

Any resonant solution to the cavity condition with the same spatial profile, called a longitudinal mode, will be separated in frequency space by the Free Spectral Range (FSR) given by $\nu_f = c/2l$. These cavity modes are well approximated by solutions to the paraxial Helmholtz equation, the paraboloidal wave and the Gaussian beam. The rest of this section will focus on the Gaussian beam solution, which can be written as [Saleh and Teich, 2007]

$$U(\vec{r}) = \frac{W_0}{W(z)} exp[\frac{\rho^2}{W^2(z)}] exp[-ikz - ik\frac{\rho^2}{2R(z)} + i\chi] \tag{4.11}$$

where

$$W(z) = W_0\sqrt{1 + (\frac{z}{z_0})^2}, \tag{4.12}$$

$$R(z) = z[1 + (\frac{z_0}{z})^2], \tag{4.13}$$

$$\chi = \tan^{-1} \frac{z}{z_0}, \tag{4.14}$$

$$z_0 = \frac{\pi W_0^2}{\lambda} \tag{4.15}$$

and W_0 is the mode waist, W_Z is the beam size at position z, $R(z)$ is the Radius of curvature (ROC), χ is the Gouy phase and z_0 is the Rayleigh length. The mode waist, W_0, is the smallest the Gaussian beam radii can be and it grows by $\sqrt{2}$ at the Rayleigh range. As this applies to both positive and negative directions on the paraxial axis, there is a $2z_0$ range known as the depth of focus. Furthermore, our hemispherical cavity design means the Gaussian beam must match our curved mirror's ROC at a given cavity length d such that $R_1(z = d) = d(1 + (z_0/d)^2)$.

In addition to the cavity length and mirror ROC, an optical cavity's performance is defined by the total *loss* in the system. I have italicized *loss* because there are designed losses in a cavity, via transmission in the cavity defined Gaussian mode, and undesirable losses, from the mirrors' finite aperture size, absorption losses and scattering. The cavity performance can be quantified by its Finesse parameter where L^* is the cavity's total loss.

$$F = 2\pi \frac{\sqrt{1 - L^*}}{L^*} \tag{4.16}$$

The Finesse controls the cavity's decay rate, κ, which can be written as a function of the FSR and the Finesse

$$\kappa = \pi \nu_f / F \tag{4.17}$$

Currently, κ is an all encompassing term that describes both designed transmission losses and undesirable losses, via scattering, absorption or aperturing. As such, we will decompose $\kappa = \kappa_L + \kappa_R + \kappa_B$ where κ_L and κ_R denote transmission losses from either the left or right mirror respectively. κ_B will represent all the additional losses in the system. As we will see in the next section, κ is an important parameter for defining a cavity QED system.

4.2.1 The *Bad* Cavity Regime

From sections 4.1 and 4.2.1, we have defined three relevant rates that characterize a cavity QED system, the ion-cavity coupling strength g (Eq. 4.3), the cavity decay rate κ (Eq. 4.17), and the atom's spontaneous emission rate Γ (Eq. 4.9). These three rates can be combined into the ion-cavity coupling parameter known as the cooperativity C given by:

$$C = \frac{g^2}{\kappa\gamma} \tag{4.18}$$

When C>1, the system is in the strong coupling regime where the photons emitted by the ion are more likely to continually be reflected inside the resonator until they are reabsorbed by the ion. When C<1, the system is in the weak coupling regime, where the emitted photon is more likely to be emitted outside of the cavity instead of being reabsorbed. We will focus on the weak coupling regime, which Law and Kimble, 1997 refer to as the *bad* cavity regime. We call this the *bad* cavity regime because the cavity is designed such that $\kappa \gg g^2/\kappa \gg \Gamma$ where the primary decay rate is outside of the cavity. The cavity is intentionally leaky but the leaking occurs into the preferred Gaussian optical mode. The leaking must be significantly faster than the spontaneous emission rate for the $2S_{1/2} \rightarrow 2P_{1/2}$ of $^{171}Yb^{+}$ at $\Gamma = 2\pi \times 19.6MHz$.

To operate in the *bad* cavity regime, we create a small volume microcavity with designed transmission losses to collect the photon. The effective mode volume for a Gaussian beam is calculated as $V = \int |U(\vec{r})|^2 dr$. For a Gaussian mode with waist W_0 and cavity length d, this evaluates to $\pi W_0^2 d/4$. As the Gaussian beam propagates within the cavity, the field amplitude is reduced by $W_0/W(z)$, decreasing the vacuum Rabi oscillation strength g. Thus, we will design our cavity to have the ion sit at a the maximum field strength, within the depth of focus (z_0) for the cavity. Increasing κ either requires shortening the cavity length or decreasing the Finesse. Shortening the cavity length comes at a cost, as a large dielectric surface near the ion leads to increased ion heating rates [Teller et al., 2023]. The alternative option is to have a high transmission mirror to emit photons and also decrease

the overall Finesse.

The photon generation rate is an ion's intrinsic property that we derived with Wigner-Weisskopf theory in section 4.1. In the 1940s, E.M. Purcell discovered that by coupling an ion to a resonant cavity, photon emission rate can be enhanced [Purcell, 1946]. As shown in Eq. 4.8, the excited state decay rate is proportional to the density of states for the surrounding space. When the ion is surrounded by a cavity, the density of states increases from the free space density of states $D_{free}(\nu) = L^3\nu^2/\pi^2c^3$ to

$$D_{cav}(\nu) = \frac{\kappa}{\pi V}\frac{1}{\kappa^2 + (\nu_{cav} - \nu)^2} \tag{4.19}$$

where ν_{cav} is the cavity resonance angular frequency and ν is the atomic transition angular frequency [Francs et al., 2016]. Comparing these two gives the Purcell enhancement factor [Barnes et al., 2020]

$$F_p = \frac{3Q\lambda^3}{4\pi^2 V} \tag{4.20}$$

where the quality factor Q is an alternative way to characterize a resonator and is described by the resonance frequency (ν_0) divided by the resonator's linewidth ($\delta\nu$), $Q = \nu_0/\delta\nu$. The Purcell factor quantifies the spontaneous emission rate enhancement and is related to the cooperativity by $F_P = 2C$.

In the long time limit, the total emission probability that a single photon leaks out of a cavity is given by Cui and Raymer, 2005

$$P = \frac{C}{C+1}\frac{\kappa_L}{\kappa + \Gamma}. \tag{4.21}$$

The first term describes the probability the photon is emitted into the cavity mode without making a spontaneous atomic decay. The second term is the probability we measure said photon. Note, the numerator defines κ_L. In this leaky cavity design, photons can only be efficiently collected on one side of the cavity, which we have denoted as the left mirror in this equation.

4.3 MicroMirror Fabrication

The key ingredients for an effective Fabry-Perot interferometer are good mirrors. Furthermore, as shown in Section 4.1, smaller mode volumes increase the potential photon collection efficiency to over 50 percent. Micromirrors can achieve this mode volume if one can devise an effective method to fabricate them.

4.3.1 CO_2 Ablation Process and Surface Characterization

Using a spatially filtered 25W Synrad 48-2W 10.6μm laser, we ablated a crater onto an optically polished Valley Design fused silica substrate. The crater has near-spherical geometry and subsequent low-power melting pulses can achieve subnanometer surface roughness (denoted σ henceforth) [Nowak et al., 2006]. The fraction of total reflected radiant power remaining in a specular beam after reflection on a single moderately rough surface is given by $R_s/R_t = exp[-(4\pi\cos\theta_i\sigma/\lambda)^2]$, where R_s and R_t are the specular reflectance and total reflectance respectively, θ_i is the incidence angle and λ is the light wavelength. It follows that the Total Integrated Scatter (TIS) can be described by [Harvey et al., 2012]

$$TIS = 1 - exp[-(4\pi\cos\theta_i\sigma/\lambda)^2]. \tag{4.22}$$

Surface roughness can be directly inferred by summing over the product of surface's power spectral density (denoted PSD henceforth), ($\hat{S}_1(f_k)$, at set spatial frequencies.

$$\sigma^2 = \frac{2}{Nd}\sum_{k=k_{min}}^{k_{max}} \hat{S}_1(f_k) \tag{4.23}$$

where N is the number of points and d is the spacing between successive PSDs. The factor of 2 comes from only considering one side of the symmetrical PSD function [Stover, 1995]. The two-dimensional PSD can be defined by

$$S(f_x, f_y) = \lim_{L\to\infty}\frac{1}{L^2}\left|\int_{-L/2}^{-L/2}\int_{-L/2}^{-L/2} z(x,y)e^{-j2\pi(f_x x + f_y y)}dxdy\right|^2 \tag{4.24}$$

where L is the scan length, $z(x,y)$ is the height function of the surface, and $f_x(y)$ is the

spatial frequency. Practically speaking, measuring L out to infinity is impossible, so we can consider the PSD as a summation

$$S(f_x, f_y) = L^2[\frac{1}{N^2}\sum_{n=0}^{N}\sum_{m=0}^{N} z(x_m, y_n)e^{-2\pi j x_m f_x}e^{-2\pi j y_m f_y}]^2 \tag{4.25}$$

where $x_m = m\frac{L}{N}$ and $y_m = n\frac{L}{N}$ and the spatial frequencies take the discrete range of values [Gavrila et al., 2006]

$$f_x, f_y \ = \frac{1}{L}, \frac{2}{L}, ..., \frac{N}{2L}$$

.

To characterize the crater and the surface quality, we used three well-known characterization techniques: white light profilometry, atomic force microscopy, and laser confocal microscopy.

4.3.2 Atomic Force Microscopy

Developed by Binnig et al., 1986, atomic force microscopy uses a cantilever with a sharp tip to scan over a sample surface. As the probe scans across the same surface, attractive or repulsive forces between the tip and the sample cause deflection of the cantilever. In a tapping mode, the mode utilized in the subsequent data collection, the cantilever is oscillated at its fundamental resonance frequency and any deviations in the oscillation frequency or amplitude provide information about the surface topology. Although a powerful technique for identifying vertical atomic features on the pm scale [Hoogenboom et al., 2006], the contact with the surface can result in tip damage or surface damage, making this a potentially destructive process for surface characterization [Khan et al., 2016].

4.3.3 Coating and Mirror Characterization

Mirror coatings have been optimized by many commercial vendors, including but not limited to Advanced Thin (AT) Films and FiveNine optics, to achieve reflectances at 0.001%. We sent the aforementioned micromirrors to be coated by AT films with the coatings shown in Figure 4.1. The coating at 370 nm is designed to follow our leaky cavity regime, where

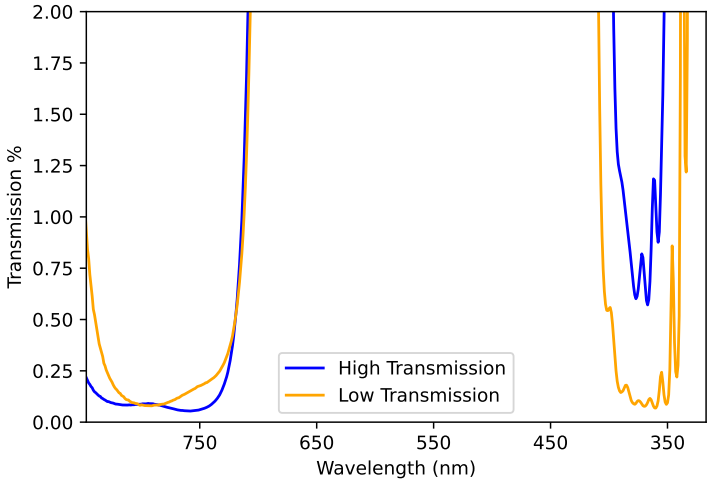

FIGURE 4.1: Measured transmission curve (in percent) from AT films

the High Transmission side is intended for photon collection. At infrared wavelengths, we also have a similar coating for cavity stabilization in situ at the commonly used industry standard Rubidium transition $5S_{1/2} \rightarrow 5P_{1/2}$ line at 384.2279819 THz [Kraft et al., 2004]. Once the mirrors were coated, we can measure the 'bad losses' via a diagnostic cavity, with 20 cm Radius of Curvature mirrors. We test the cavity by sending 780 nm light that has been phase modulated by a fiber EOSpace electro-optic modulator (EOM) set to $f_{mod} = 2.1GHz$ measuring the transmission signal on a Thorlabs PDA36A2 Si Free-space amplified photodiode. The same measurement was repeated at 370 nm modulated by a free space Qubig $f_{mod} = 1.5GHz$ EOM. By scanning the cavity length via a piezoelectric transducer, we can see a characteristic linewidth with distinct sidebands separated by the modulation frequency shown in Figure 4.2.

The linewidth can be fit with a Lorentzian function

$$L(x) = \frac{1}{\pi} \frac{\frac{1}{2}\Gamma}{(x - x_0)^2 + (\frac{1}{2}\Gamma)^2} \tag{4.26}$$

where Γ is the linewidth in time domain. Using the modulated sidebands as a time domain to frequency domain conversion ruler, and comparing the linewidth to the FSR, we can

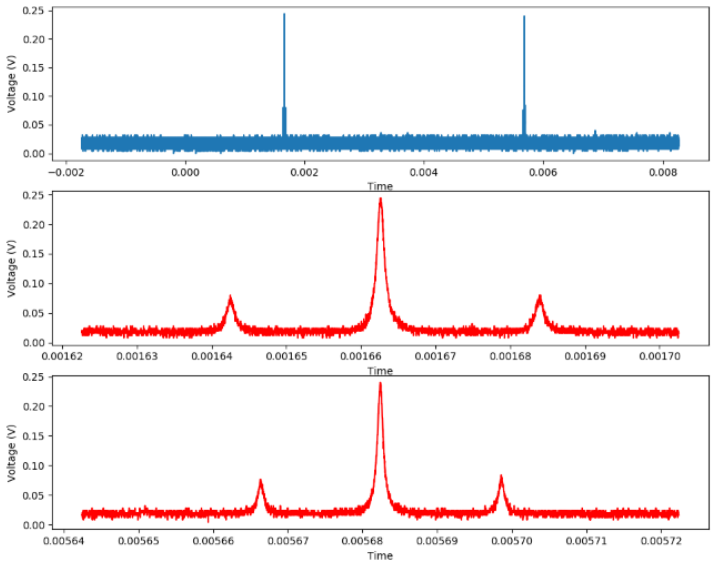

FIGURE 4.2: **Scanned free spectral range of cavity in time domain (ms).** a) Time scan of linewidth at 780nm with 2.1 GHz modulated sidebands. b) Zoom in of the left peak in FSR. c) Zoom in of the right peak in FSR.

Table 4.1: Measured coating losses at 780 and 370 nm for High/Low Transmission AT films coating

Wavelength (nm)	Cavity Mirror 1	Cavity Mirror 2	Finesse	Scattering Losses
370	T=1020 ppm	T=1020 ppm	2932	51 ppm
370	T=7304 ppm	T=1020 ppm	735	179 ppm
780	T=764 ppm	T=1102ppm	3355	3 ppm

obtain the cavity finesse.

$$\text{Finesse} = \frac{FSR}{\Gamma} \tag{4.27}$$

The first step in our characterization is testing the coating. Using the diagnostic mirrors, which we assume have negligible surface roughness, we can estimate the coating's scattering losses. These results, shown in Table 4.1, set an upper bound of the cavity quality.

Next, we need to test the micromirror Finesse. The test setup involves one diagnostic 20 cm mirror as the flat surface and a micromirror forming a semispherical cavity. Unlike the

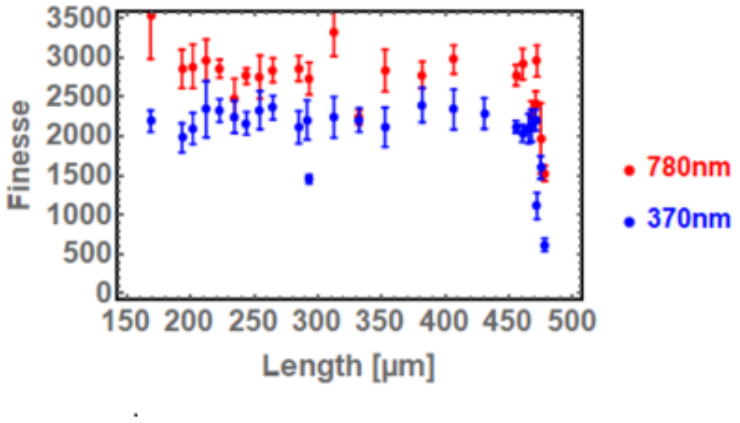

FIGURE 4.3: **Micromirror Finesse Measurements.** The cavity exhibits nearly the same Finesse over the entire cavity length until the stability condition.

diagnostic mirrors, we need to characterize the interferometer up to the stability condition because we want to optimize the ion-cavity mode coupling which, as shown in section 4.1, is preferred at the cavity mode waist. Thus, we repeat the linewidth measurement at our two characteristic wavelengths, 780nm and 370nm, over the entire cavity length. As shown in Figure 4.3, the cavity exhibits a steep falloff in finesse at 477 μm. For this particular micromirror, this is the stability condition being broken, indicating an effective ROC of approximately 477 um. To measure the small cavity length precisely, we use two similar wavelengths at 780nm, one locked to a Rubidium spectroscopy signal and another unlocked at around 300 GHz away. The large free spectral range makes any MHz drift in the laser result in an inaccuracy of the cavity estimation by $\leqslant 1\mu m$. We can repeat this measurement at two 370nm frequencies that are also separated by 300 GHz. If the two wavelengths' linewidth for the same order Gaussian TEM mode overlap, then we know the cavity's FSR is the laser frequency separation. However, these micro-cavities have a typical FSR $\geqslant 300GHz$, which in practice is outside the tunable range for most external cavity diode lasers (ECDLs).

An alternative way to measure the FSR involves a very similar experimental approach. We propagate two nearly identical wavelengths into the interferometer, where only the TEM_{00} is transmitted. The wavelength separation needs to be greater than the cavity

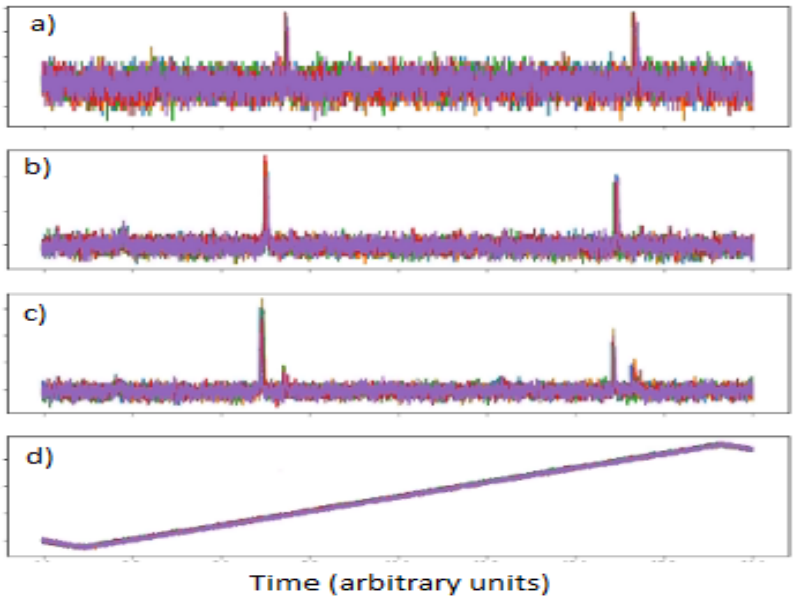

FIGURE 4.4: **FSR measurement at 370nm.** a) Oscilloscope trace for laser 1. b) Oscilloscope trace for laser 2, frequency separated by 0.39040 GHz. c) Oscilloscope trace for both lasers 1 and 2. d) Voltage ramp for cavity length scan. All traces are collected in time domain which has been omitted as it is not relevant for this measurement. Only the peak location is critical.

linewidth ($\approx$ 100 MHz) and less than the FSR. On a photodiode, the transmitted signal is shown in Figure 4.4. Identifying the peak locations as $N\frac{\lambda_i}{2}$ and $(N+1)\frac{\lambda_i}{2}$, we can determine N from equation 4.28.

$$N = \frac{\lambda_1}{\lambda_2 - \lambda_1}\frac{T_2}{T_1} \tag{4.28}$$

4.4 Surface Trap and UHV Integration

From Sandia National Labs, we received a surface trap fabricated on an AT films coated substrate. The trap has a 11 μm radii aperture gap in the electrodes to serve as half of our semispherical cavity. Using a micromirror, we can create a new cavity to test the mirror quality post trap fabrication. These results are shown in Figure 4.5.

Comparing to 4.3 at 370nm, we see two distinct features. First, the overall finesse has decreased to 1400 ± 200 which could be attributed to additional roughness accrued during

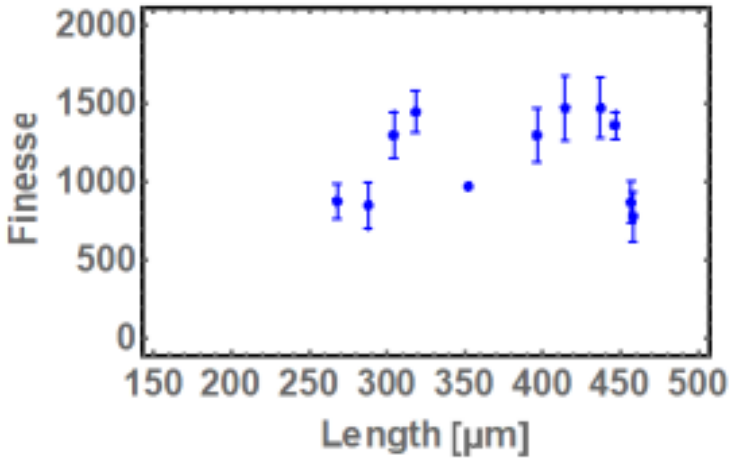

FIGURE 4.5: **370 nm cavity measurements with Sandia surface trap.** The surface trap has an expected transmission of 1020 ppm. Large finesse loss attributed to aperture clipping and imperfect cavity alignment.

the fabrication process. If we maintain our scattering model from Eq. 4.22, the surface would be rougher by 1.1 nm. However, this explanation does not explain the significant losses seen at 250μm. A more likely explanation is the limitation enforced by the aperture on the cavity alignment. In Figure 4.6, we simulate the 370 nm cavity with a FoxLi numerical simulation. Figure 4.6 **a** shows as the cavity length gets smaller, the Gaussian mode waist increases, leading to mode clipping that is maximized at cavity $l = ROC/2$. In Figure 4.6 **b**, we also see that if the trap aperture is offset by 5μm, there is a steep fall off in the maximum finesse. Combining these two effects could explain the measured Finesse shown in Figure 4.3. Unfortunately in this particular diagnostic setup, we did not have fine μm control of either the micromirror or the trap aperture. We added this functionality in the future design iterations.

4.4.1 Cantilever Design

An optical cavity that is compatible with an ultra-high vacuum environment should be flexible enough to allow for independent ion trap verification with and without the Fabry-

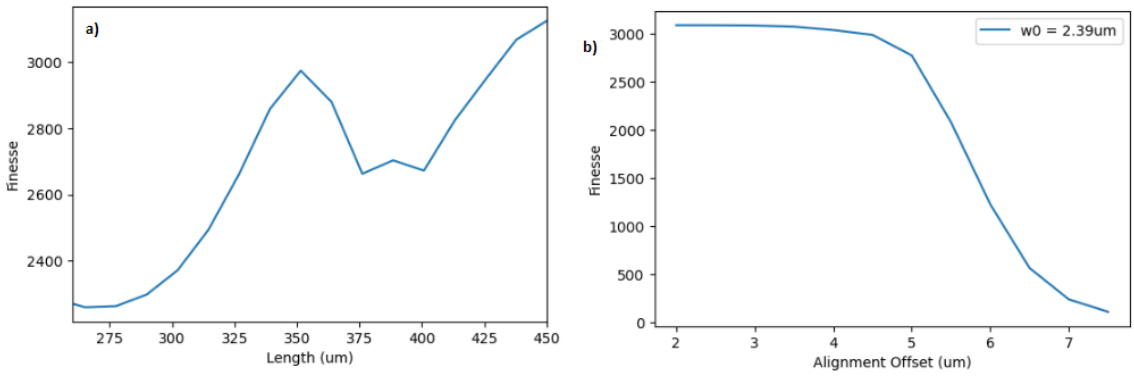

FIGURE 4.6: **370 nm FoxLi Simulation.** a) Using a 470 μm ROC mirror, simulated cavity Finesse as a function of cavity length using a FoxLi simulation with 600 iterations. b) Simulated alignment offset with a 11 μm cutoff aperture.

Perot cavity, but robust enough to precisely control the micromirror location within a micron. We epoxied a micromirror to a three-axis xyz cantilever composed of two SmarAct SL-0610 and one SC-1720 as shown in Figure 4.7. The two smaller (SL-0610) stages have 1 nanometer resolution but only 4.5 mm of travel range while the last SC-1720 provides enough travel distance to completely remove the micromirror. The entire bracket was custom designed with titanium Grade 2 to minimize outgassing. On the right side of the bracket, a Physics Instruments PL022 piezo is epoxied to adjust the cavity length over the FSR. Stainless steel 316 screws are inset into the micromirror bracket for larger cavity length adjustments. Inside the center of the titanium bracket and below the micromirror, the CPGA with an affixed surface trap is connected (not shown) which has a flat coated surface to act as the other half of our hemispherical cavity.

4.4.2 Mode Matching

Typically Gaussian mode matching to an optical cavity is relatively straightforward: the cavity mirror geometry defines a preferential mode of propagation and the input light should match the mode. The overlap integral between these two modes, E_1 and E_2, written as

$$\eta = \frac{|\int E_1 * E_2 dA|^2}{\int E_1^2 dA \int E_2^2 dA}, \tag{4.29}$$

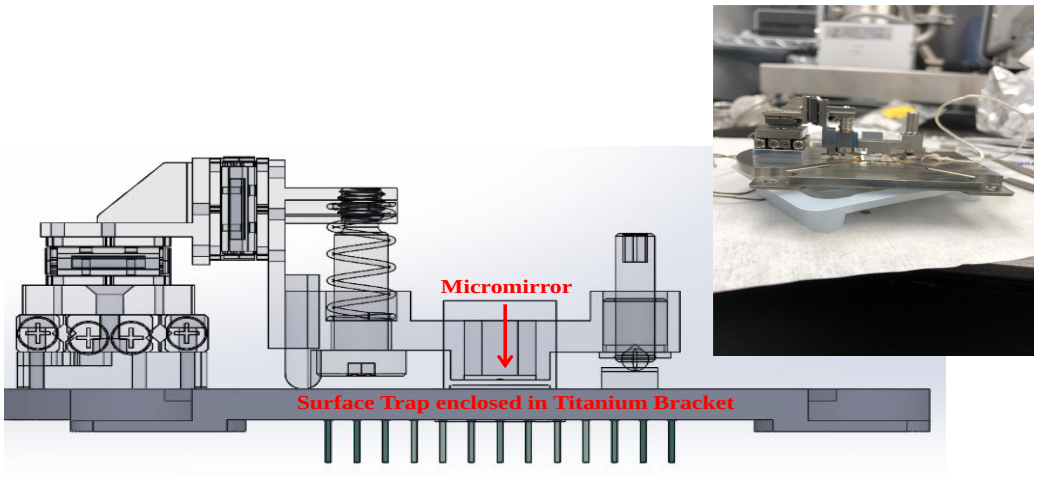

FIGURE 4.7: **Titanium Bracket with three axis cantilever.** CAD drawing of test micromirror setup. Actual bracket used shown in upper right corner.

defines the coupling efficiency, η, between the input light and the cavity. In an ultra-high vacuum chamber, there are engineering constraints that remove degrees of freedom which affect the input light's spatial profile. I will discuss these constraints and the simulated mode matching in the following section.

4.4.2.1 Zemax Modeling

In order to trap an ion, the bracket shown in Figure 4.7, needs to be placed into an ultra-high vacuum environment similar to the octagon shown in Fig 3.1. The target cavity mode waist is 2.6 μm to optimize the cooperativity shown in 4.18. The octagon limits the location of the nearest optic outside of vacuum by $\approx$ 20 mm. Mode matching to this target waist would force the input light to be a few *mms*. At this waist size, imperfect optic radii of curvature can affect the wavefront significantly, potentially acting as finite aperture sizes and creating airy disks at the focal plane. The solution is to minimize the distance between the cavity mode and nearest optic, which requires a lens within vacuum.

By placing a lens in vacuum, illustrated in Fig 4.8, we sacrifice the ability to adjust the lens' lateral location relative to the optical cavity. We can minimize this offset by measuring

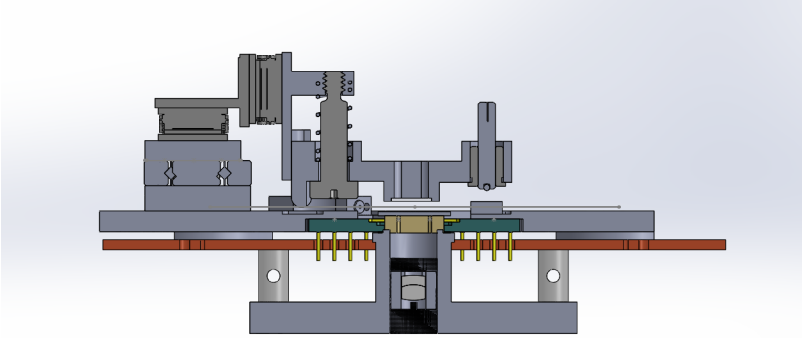

FIGURE 4.8: **Titanium lens bracket mount.** The mount grooves matches the backside of the CPGA and have fine threads to adjust the lens position

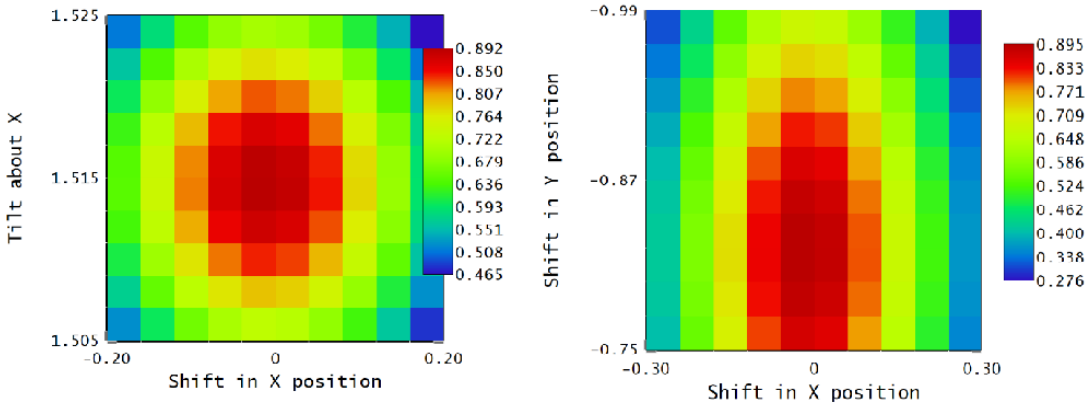

FIGURE 4.9: **Mode matching model by adjusting input light's position and tiltu.** The lens is misaligned by 0.4 mm and tilted by 0.5 degrees. Left tolerance plot shows the input light needs to be tilted within 0.02 degrees. Right tolerance plot shows the input light needs to be positioned laterally within 150 μm. Color indicates the estimated mode matching to the cavity mode.

the location of the trap relative to its affixed CPGA, however, there is still some residual misalignment on the order of 0.4 mm. We can model any misalignment and estimate the potential mode matching with Zemax OpticStudio. Using a generous misalignment of the vacuum lens by 0.4 mm and a tilt offset of 0.5 degrees, the input light can still obtain a modeled $\geqslant$80% mode matching. These results are shown in Figure 4.9. The Zemax modeling puts some stringent requirements on the input light's location and tilt, requiring the tilt be adjusted within 0.02 degrees and the light adjusted by 150 μm. This required a non-conventional optomechanical design.

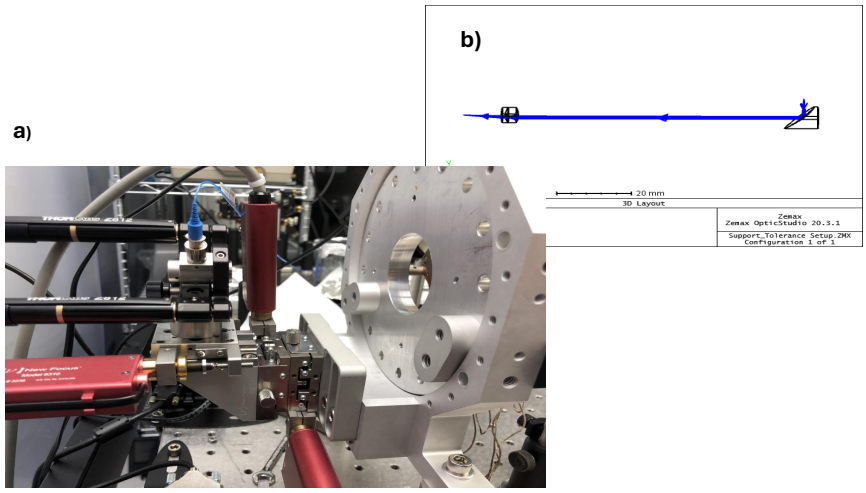

FIGURE 4.10: **Optomechanical design for coupling into Ultra High Vacuum with Zemax model.** a) Physical implementation of optomechanical design for precise cavity coupling. The steel stage is outfitted with three Newport 9910 stages for precise positioning of the reflective collimator. The reflective collimator is inset in a Kinematic motorized stage for small tilt adjustments. b) Zemax model used to determine estimated modematching and tolerance analysis.

Our final optomechanical design, shown in Figure 4.10 used a reflective collimator to remove achromatic effects between two wavelengths 399 nm and 370 nm. The original 780 nm reference wavelength became too troublesome to incorporate due to the large focal shifts between 780 nm and 370 nm for most off-the-shelf optics. The reflective collimator inset in a motorized Kinematic stage which was then placed on a nanometer accurate Newport 9910 stepper stages along x and y. The configuration allowed for raster scanning the input light location along four potential parameters and the experimental results can be shown in Figure 4.11.

4.4.3 Noise Characterization

To characterize the noise of our Fabry-Perot, we adjust the cavity piezo so that the interferometer is in resonance with a cavity mode. At the resonance, in principle, most of the light should be transmitted through the cavity, and any fluctuations in the transmitted light could be either from respective vibrations between the input light and the cavity or

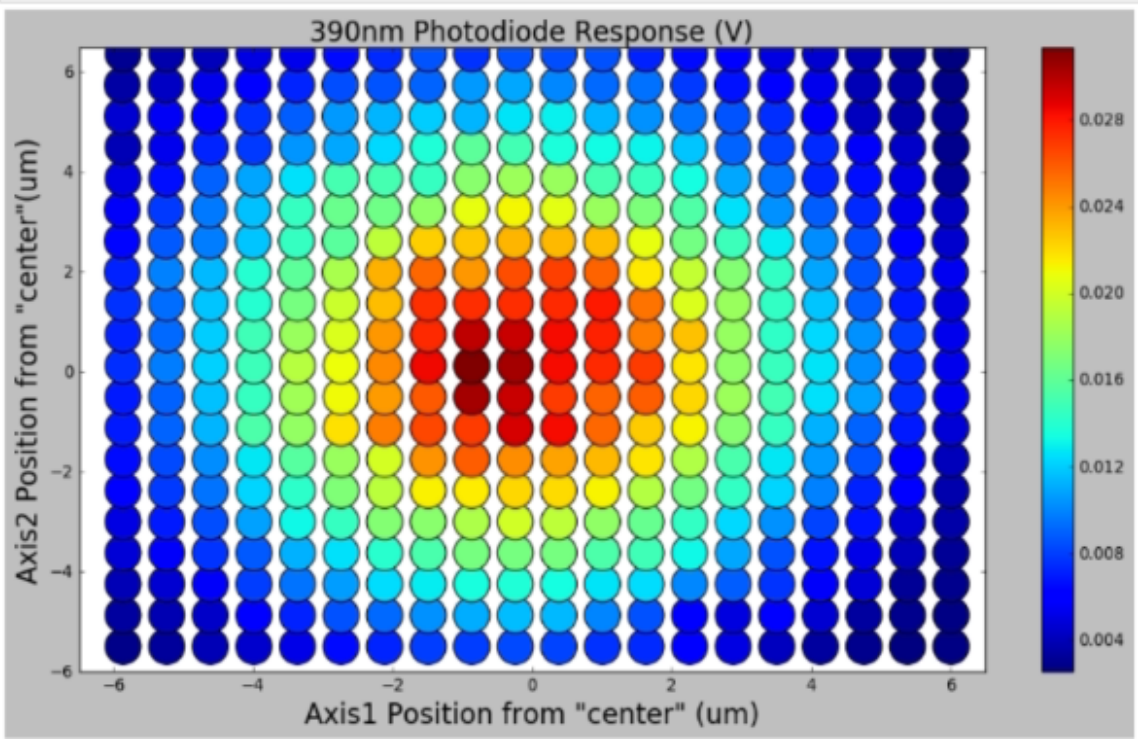

FIGURE 4.11: **Measured Mode Coupling as a function of Coupling Light Position.** The colors represent actual measured photodiode amplified output.

instability in the cavity itself. The light fluctuations were measured on a Thorlabs 36A2 photodiode and then we Fourier transformed the time series data to estimate the noise power spectral density (PSD), shown in Figure 4.12.

The power spectral density indicated two noise peaks at 330 Hz and 600 Hz which made the cavity fluctuate from on resonance to completely off resonant. This meant that the cantilever design caused the cavity to be unstable. Attempts to suppress the noise were unsuccessful.

4.5 Future Steps

The cavity design outlined in this chapter showed some of the considerations needed to install an interferometer in vacuum. The large distance between the external view-port and the interior cavity location set a fundamental limit due to Gaussian optics. There are only two ways to address this, large Gaussian beams which can sample imperfections in off-the-shelf optics or fixed lenses within vacuum which do not have any degrees of freedom.

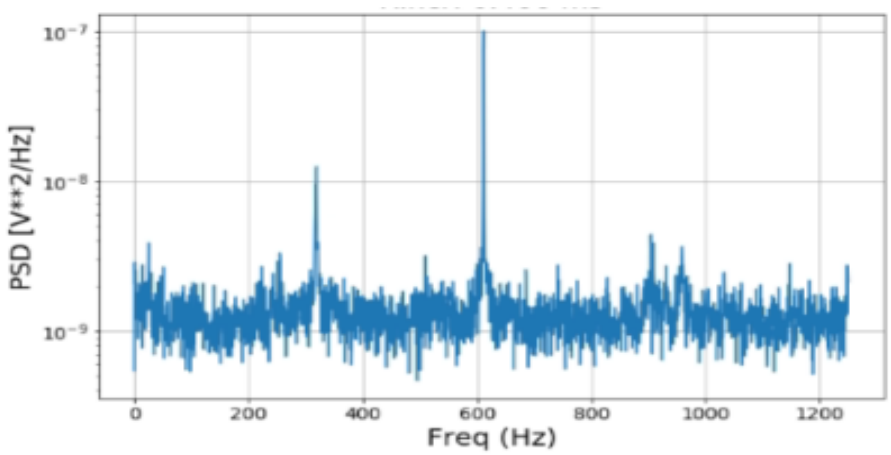

FIGURE 4.12: **Measured Power Spectral Density from Cavity Transmission Signal.** There are two key noise peaks we measure from our cavity signal at ≈330 Hz and 600 Hz. We can identify these noise sources from the analysis of our cantilever design.

Although we overcame this problem with an internal lens, this is still inherently problematic as it sets tight tolerances on the input light and puts an upper threshold of the input-to-cavity coupling. A better design would have negligible distance between the cavity location and the input optics, making input coupling significantly more straightforward.

Secondly, the cavity itself needs to be composed of a fixed structure, instead of the flexible cantilever proposed in this work. Such a fixed structure removes the possibility of movement between the respective mirrors, and addresses the noise problem we measured. To align such a cavity, semi-conductor technology has developed precise alignment marks that can set separate substrates within 1 μm. A similar technique was used during the fabrication of the surface traps we use. Fabricating the entire cavity with one substrate being the surface trap and the second being the micromirror in a semi-conductor fab using these alignment marks as a guiding reference will make the alignment seamless and robust.

5. Tools for Quantum Simulation

In Chapter 2, we illustrated some of the tools available to trapped ions to conduct quantum simulations. In this following chapter, I discuss the utilization of these tools to explore an important chemical model, the linear vibronic coupling model (LVCM) and a particular phenomenon, the Herzberg-Teller effect, that could be observed with this model.

5.1 Implementing the Linear Vibronic Coupling Model

5.1.1 Trotterization

There are two predominant methods for mapping a chemical model, such as the linear vibronic coupling model, onto a trapped ion system; analog quantum simulators and Trotterized circuit implementation. An analog quantum simulator maps each term of the Hamiltonian onto a component within the trapped ion hardware. The system is allowed to evolve over time, providing a one-to-one correlation between the target model dynamics and the simulator itself. For the LVCM model, a recent result demonstrated an analog quantum simulator illustrating the time dynamics for photoexcited pyrazine, allene and butatriene [et al., 2024]. However, analog quantum simulators require every component in the Hamiltonian to be driven simultaneously. Furthermore, if terms in the Hamiltonian are time-dependent, as we will see in the following sections, these changes need to be made in real time to correlate with the target Hamiltonian. In practice, for a trapped ion system, this puts a large overhead on the lasers needed to drive the respective Raman transitions especially as chemical dynamical models become more complex.

Alternatively, Trotterized circuit implementation separates the Hamiltonian into small unitary operations, where each individual term is driven for a short time step. These time steps are only a portion of the total time evolution. The unitary operations are then repeated for each term in the Hamiltonian until the desired time evolution. For the LVCM model we implement, we can write in the interaction picture

$$\hat{H}_I(t) = \hat{H}_I^{(1)}(t) + \hat{H}_I^{(2)}(t) \tag{5.1}$$

where

$$\hat{H}_I^1(t_j) = \frac{\alpha}{2}\hat{\sigma}_x(t_j) + \frac{\Delta}{2}\hat{\sigma}_y(t_j) \tag{5.2}$$

$$\hat{H}_I^2(t_j) = \frac{\kappa}{2}(\hat{\sigma}_x + \hat{\sigma}_y)(\hat{a}e^{-i\nu t_j} + \hat{a}^\dagger e^{i\nu t_j}) \tag{5.3}$$

We can denote the target time evolution $\hat{U}_{target}$ where

$$\hat{U}_{target}(T) = \mathcal{T}exp(-i\int_0^T \hat{H}_I(t')dt' \tag{5.4}$$

and $\mathcal{T}$ is the time-ordering operator, sorting each operator into chronological order. [Sun et al., 2023] The Trotterized form of the time evolution then takes the form of

$$\hat{U} = \hat{U}_N\hat{U}_{N-1}...\hat{U}_1 = \hat{U}_{target}(T) + O[(T/N)^2] \tag{5.5}$$

where each step in the Trotterization is represented by a first-order Trotter formula

$$\hat{U}_j = e^{-i\hat{H}_I^1(t_j)\frac{T}{N}}e^{-i\hat{H}_I^2(t_j)\frac{T}{N}}. \tag{5.6}$$

Equation 5.5 indicates an error in the Trotterization approach that is not present in the analog operation. This error is due to a fundamental non-commuting aspect of operators in the interaction Hamiltonian

$$Error \approx \frac{\Delta t^2}{2}[H_I^{(1)}, H_I^{(2)}] \tag{5.7}$$

The error can be mitigated by either increasing the number of steps in the Trotterization or moving to second order Trotterization, where the error scales as $O[(T/N)^3]$.

To achieve the Trotterization in practice, at each time step, the motion phase for the SDK (Equation 5.3), is set to be νt_j, where $t_j \equiv (j-1/2)\frac{T}{N\tau}$, τ the duration of the time step's operation and T is the total time evolution. In practice, this is done by setting the anti-symmetric detuning from the sideband transitions for each time step. For the single qubit terms, (Equation 5.2), the operation is more straightforward. We split the single qubit's total operation into small angle rotations, θ, and adjust the laser phase, ϕ

to correlate with either a σ_x or σ_y operator. This is equivalent to each operation up to a global phase $-i$.

$$\hat{\sigma}_\phi(\theta) = \begin{pmatrix} \cos\left(\frac{\theta}{2}\right) & -i\sin\left(\frac{\theta}{2}\right)e^{-i\phi} \\ -i\sin\left(\frac{\theta}{2}\right)e^{i\phi} & \cos\left(\frac{\theta}{2}\right) \end{pmatrix} \tag{5.8}$$

Although the Trotterization approach has an intrinsic error, it allows us to execute the linear vibronic Hamiltonian through sequential steps, ideal for our setup as we only have one Raman lasers to execute transitions. The Trotterized form also allows us to adjust the Hamiltonian to match time evolving coupling terms, which will become relevant when we look at the Herzberg-Teller model in the next section. Lastly, if gives us the capability to introduce dephasing during each step in the Trotterization.

5.1.2 Herzberg-Teller Effect

The Frank-Condon approximation is a fundamental chemical principle stating molecular electronic transitions are relatively instantaneous compared to any motion of their respective atomic nuclei [Anonymous, 1926]. The exclusion of nuclear coordinates in the dipole moment of the electronic matrix element has been sufficient for assigning spectral lines in a majority of molecular systems[Kundu et al., 2022]. However, the Frank-Condon approximation has been shown to break down in some cases, most notably in aromatic molecules like free-base porphyrins [Roy et al., 2022]. Correction to account for the changes in the molecular spectra lines involve the lowest order expansion of the dipole moment matrix

$$\vec{\mu} = \langle g|\,\hat{\mu}\,|e\rangle \approx \vec{\mu}^0 + \sum_n \vec{\mu}_k^1(\hat{q}_k - \vec{q}_k^g) \tag{5.9}$$

where $\langle g|$ and $|e\rangle$ are the ground and excited electronic states, $\vec{q}$ is the vector of normal mode coordinates at the equilibrium geometry q^g, μ_0 is the coordinate-independent component of the dipole matrix element and μ_k^1 is its first derivative relative to the position q_k. The first term in the dipole expansion is responsible for Frank-Condon transitions while the vector $\vec{\mu}_k$ of dipole derivative is responsible for Herzberg - Teller coupling [Kano et al., 2002].

To observe this effect in a trapped ion simulator, we start from the light-molecule Hamiltonian,

$$\begin{pmatrix} H_g & 0 \\ 0 & H_e \end{pmatrix} + \begin{pmatrix} 0 & \vec{\mu_{ge}} \\ \vec{\mu_{eg}} & 0 \end{pmatrix} \cdot \vec{E(t)} \tag{5.10}$$

where $E(t) = \vec{\epsilon} e^{i\omega t}$. The ground state Hamiltonian in second quantized notation can be written

$$H_g = E_g \left|g\right\rangle\left\langle g\right| + \left|g\right\rangle\left\langle g\right| \otimes \sum_n \omega_n \hat{a}_n^\dagger \hat{a}_n \tag{5.11}$$

and the excited state Hamiltonian only differs from the ground state Hamiltonian via a shift in the vibrational equilibrium positions

$$H_e = E_e \left|e\right\rangle\left\langle e\right| + \left|e\right\rangle\left\langle e\right| \otimes \sum_n \omega_n (\hat{a}_n^\dagger + s_n)(\hat{a}_n + s_n) \tag{5.12}$$

$$= E_e \left|e\right\rangle\left\langle e\right| + \left|e\right\rangle\left\langle e\right| \otimes \sum_n \omega_n (\hat{a}_n^\dagger \hat{a}_n + s_n(\hat{a}_n^\dagger + \hat{a}_n) + s_n^2) \tag{5.13}$$

The key component of the Herzberg-Teller effect is expanding the dipole operator into 1st order of the vibrational coordinates, which we can write in second quantized form as (using the assumption $\vec{\mu} = \vec{\mu}_{ge} = \vec{\mu}_{eg}$)

$$\vec{\mu} = \vec{\mu}^{(0)} + \sum_n \vec{\mu}_n^{(1)} (\hat{a}_n^\dagger + \hat{a}_n) \tag{5.14}$$

Rewriting Equation 5.10 given the adjusted excited-state Hamiltonian gives us:

$$\begin{aligned} H = & \begin{pmatrix} E_g & 0 \\ 0 & E_e + \sum_n \omega_n s_n^2 \end{pmatrix} + \begin{pmatrix} 0 & 1 \\ 1 & 0 \end{pmatrix} \vec{\mu}^{(0)} \cdot \vec{E(t)} + \sum_n \omega_n a_n^\dagger a_n \\ & + \begin{pmatrix} 0 & 0 \\ 0 & 1 \end{pmatrix} \cdot \sum_n \omega_n s_n (a_n^\dagger + a_n) + \begin{pmatrix} 0 & 1 \\ 1 & 0 \end{pmatrix} \sum_n \vec{\mu}_n^{(1)} \cdot \vec{E(t)} (a_n^\dagger + a_n) \end{aligned} \tag{5.15}$$

Applying Equation 5.15 is not naturally intuitive for trapped ions, so we need a way to alter this Hamiltonian to be more friendly for our approach.

Assuming an initial state for the electronic-vibrational system

$$\rho(0) = |g\rangle\langle g| \cdot \frac{exp(\sum_n \omega_n \hat{a}_n^\dagger \hat{a}_n)}{Z} \tag{5.16}$$

where z is a normalization factor or partition function. Defining a new set of annihilation and creation operators,

$$\hat{b}_n^\dagger = \hat{a}_n^\dagger + \frac{s_n}{2}; \hat{b}_n = a_n + \frac{s_n}{2} \tag{5.17}$$

we can rewrite our Hamiltonian and initial state

$$\rho(0) = |g\rangle\langle g| \cdot \frac{exp(\sum_n \omega_n (\hat{b}_n^\dagger - s_n/2)(\hat{b}_n - s_n/2)}{Z} \tag{5.18}$$

$$\begin{aligned} H = & \begin{pmatrix} E_g & 0 \\ 0 & E_e + \sum_n \omega_n s_n^2 \end{pmatrix} + \begin{pmatrix} 0 & 1 \\ 1 & 0 \end{pmatrix} \vec{\mu}^{(0)} \cdot \vec{E(t)} + \sum_n \omega_n (b_n^\dagger - \frac{s_n}{2})(b_n - \frac{s_n}{2}) \\ & + \begin{pmatrix} 0 & 0 \\ 0 & 1 \end{pmatrix} \cdot \sum_n \omega_n s_n (b_n^\dagger + b_n - s_n) + \begin{pmatrix} 0 & 1 \\ 1 & 0 \end{pmatrix} \sum_n \vec{\mu}_n^{(1)} \cdot \vec{E(t)} (b_n^\dagger + b_n - s_n) \end{aligned} \tag{5.19}$$

Expanding the vibrational modes then simplifying our overall Hamiltonian we obtain

$$\begin{aligned} H_{HT} = & \begin{pmatrix} E_g & 0 \\ 0 & E_e \end{pmatrix} + \begin{pmatrix} 0 & 1 \\ 1 & 0 \end{pmatrix} \left(\vec{\mu}^{(0)} \cdot \vec{E(t)} - \sum_n \vec{\mu}_n^{(1)} \cdot \vec{E(t)} s_n \right) + \sum_n \omega_n (b_n^\dagger b_n) + \sum_n \omega_n \frac{s_n^2}{4} \\ & + \begin{pmatrix} -1 & 0 \\ 0 & 1 \end{pmatrix} \cdot \sum_n \omega_n \frac{s_n}{2} (b_n^\dagger + b_n) + \begin{pmatrix} 0 & 1 \\ 1 & 0 \end{pmatrix} \sum_n \vec{\mu}_n^{(1)} \cdot \vec{E(t)} (b_n^\dagger + b_n) \end{aligned} \tag{5.20}$$

This is identical to the linear vibronic coupled model and is agreeable with Trapped ions native operations. We now will take this equation and put it in an interaction picture for trapped ion notation. Let's make the following definitions to simplify the equation:

$$\alpha_n(t) \equiv \vec{\mu}^{(0)} \cdot \vec{E}(t) - \vec{\mu}^{(1)} \cdot \vec{E}(t) s_n \tag{5.21}$$

$$\kappa_n \equiv s_n/2 \tag{5.22}$$

$$\beta_n(t) \equiv \vec{\mu}_n^{(1)} \cdot \vec{E}(t) \tag{5.23}$$

Letting our Hamiltonian of a single motional mode, ignoring the constant term and setting the zero point energy $\Delta/2$ between E_g and E_e

$$\begin{aligned} H_n = \frac{\Delta}{2}\begin{pmatrix}1 & 0\\ 0 & -1\end{pmatrix} + \alpha_n(t)\cdot\begin{pmatrix}0 & 1\\ 1 & 0\end{pmatrix} + \omega_n(b_n^\dagger b_n) \\ -\kappa_n(b_n^\dagger + b_n)\cdot\begin{pmatrix}1 & 0\\ 0 & -1\end{pmatrix} + \beta_n(t)(b_n^\dagger + b_n)\cdot\begin{pmatrix}0 & 1\\ 1 & 0\end{pmatrix} \end{aligned} \tag{5.24}$$

Moving to the interaction picture with the Hamiltonian and only considering one motional mode

$$H_D = \frac{\Delta}{2}\begin{pmatrix}1 & 0\\ 0 & -1\end{pmatrix} + \omega(b^\dagger b) \tag{5.25}$$

When we consider each time step τ_j, our interaction Hamiltonian takes the form,

$$H_I(\tau_j) = \alpha(\tau_j)\hat{\sigma}_\phi + \beta(\tau_j)\hat{\sigma}_\phi(\hat{b}^\dagger e^{i\omega t} + \hat{b}e^{-i\omega t}) - \kappa\begin{pmatrix}1 & 0\\ 0 & -1\end{pmatrix}(\hat{b}^\dagger e^{i\omega t} + \hat{b}e^{-i\omega t}) \tag{5.26}$$

where

$$\hat{\sigma}_\phi = e^{i\Delta t_j}\hat{\sigma}^- + e^{-i\Delta t_j}\hat{\sigma}^+ \tag{5.27}$$

There is an alternative approach for implementing this Hamiltonian. If we instead take Equation 5.24 and conjugate with $R_x(\pi/2)$, our one mode Hamiltonian takes the following form where $R_x(-\pi/2)\sigma_z R_x(\pi/2) = \sigma_y$ and $R_x(-\pi/2)\sigma_x R_x(\pi/2) = \sigma_x$.

$$H = \alpha(t)\hat{\sigma}_x + \frac{\Delta}{2}\hat{\sigma}_y + \omega\hat{b}^\dagger\hat{b} - \kappa\hat{\sigma}_y(\hat{b}^\dagger + \hat{b}) + \hat{\sigma}_x\beta(t)(\hat{b}^\dagger + \hat{b}) \tag{5.28}$$

Then our interaction picture will be just the vibrational frequency $\hat{H}_D = \omega(\hat{b}\hat{b}^\dagger)$ and our final Hamiltonian takes the form

$$H_I = \alpha(t)\hat{\sigma}_x + \frac{\Delta}{2}\hat{\sigma}_y + -\kappa\hat{\sigma}_y(\hat{b}^\dagger e^{i\omega t} + \hat{b}e^{-i\omega t}) + \beta(t)\hat{\sigma}_x(\hat{b}^\dagger e^{i\omega t} + \hat{b}e^{-i\omega t}) \tag{5.29}$$

We seek to apply this Hamiltonian on our trapped ion simulator, this Hamiltonian is identical to two single qubit terms and two spin coherent kicks, Equation 5.3. By simplifying the coherent kicks spin operator into the form

$$(\hat{\sigma}_x + \hat{\sigma}_y)(\hat{b}^\dagger e^{i\omega t} + \hat{b}e^{-i\omega t}) = \hat{\sigma}_\phi(\hat{b}^\dagger e^{i\omega t} + \hat{b}e^{-i\omega t}) \tag{5.30}$$

where $\hat{\sigma}_\phi$ is defined by Equation 5.8.

5.1.3 System Calibrations

We are looking to implement Equation 5.29 via the Trotterization method described in Section 5.1.1. The system operation involves conjugation at the beginning (end) of the circuit via $R_x(-\pi/2)$ ($R_x(+\pi/2)$). The conjugation is followed by Trotterized single qubit (SQ) and spin dependent kick terms (SDK), as shown in Figure 5.4. Trotterizing the Hamiltonian leads to some practical considerations to accurately portray the dynamics. These can be split up into three primary sections, AC stark shift, precise motion frequency calibration, and phase tracking between SQ and SDKs. Only by careful consideration of all three components, with precision accuracy within hundreds of Hz for the stark shift and motion frequency, does the trapped ion dynamics emulate the target Linear Vibronic Coupling Hamiltonian.

5.1.3.1 Stark Shift

A Stark shift is the change in an electronic energy level as a result of the presence of an external electric field. The shift in the energy level, if not accounted for, will correspond to an additional σ_z operator in our intended circuit. Typically, for the SQ gate, the light shift is trivial to account for. When we calibrate for the gate frequency, the laser is set to the

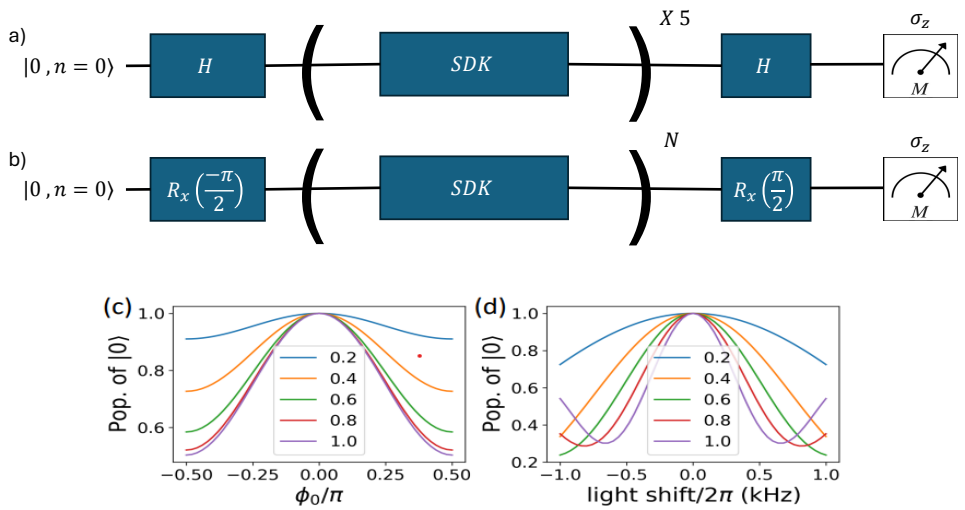

FIGURE 5.1: **Circuit models to characterize two tone light shift with simulated Hadamard light shift calibration result.** a) Hadamard circuit with 5 Trotterized SDK operations, on resonance. Motion angle is shifted by π for each succesive SDK operation in the Trotterization. b) $X(\pi/2)$ conjugated circuit with N Trotterized SDK operations, at arbitrary motion detuning ($\approx 2 \times \pi \times 8kHz$). The results of this circuit are shown in Figure 5.2. c) Scanning the spin phase of the SDK operation assuming zero light shift. The SDK operation has to be an eigenvector of the prepared eigenstate of the Hadamard. d) Scanning the light shift of the SDK operation, assuming zero spin phase offset of the SDK operation.

circuit's intended power, and the stark shift is included in the carrier frequency. The laser power consist of *one* global tone and one individual tone for this gate. When we then swap to the SDK operation, as we do in each Trotterization step, the laser power is adjusted to *two* global tones, one tone for a red sideband and one tone for a blue sideband. This results in the stark shift changing during the SDK, and it needs to be calibrated independently.

We devised two methods to calibrate the two tone SDK stark shift, shown in Figure 5.1 and 5.2. The first method conjugates the circuit with a Hadamard then uses an on resonant spin dependent kick over five Trotterization steps. Each step in the Trotterization adjust the motion phase by π so that the circuit does not end in a very large phonon number. As shown in Figure 5.1c, this conjugation is very sensitive to the spin phase ϕ_0 derived in

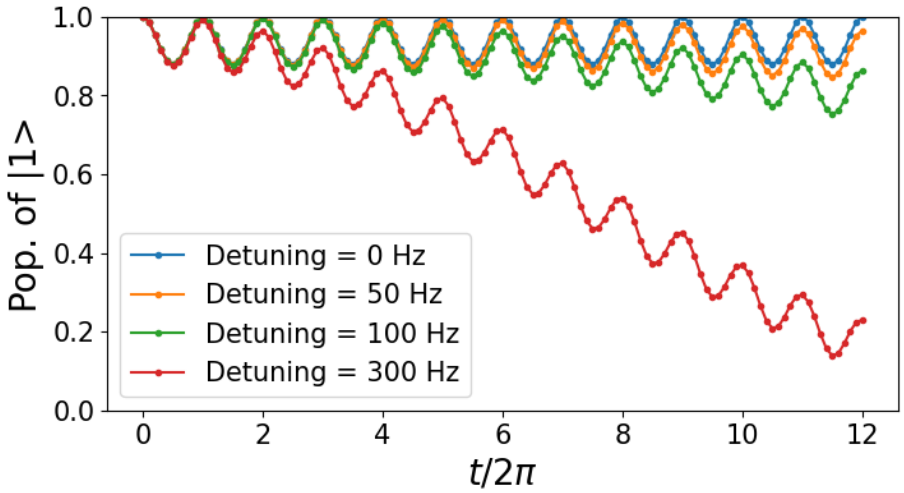

FIGURE 5.2: **Depiction of model Trotterized SDK with two tone Stark Shift.** By changing the Stark shift detuning, there is a clear shift in the dynamics curve which is sensitive to <100 Hz. When adjusting the spin phase of the SDK, the contrast diminishes, but the overall slope in the curve due to the Stark shift is still present, making this method insensitive to the spin phase.

Equation 5.3.

The alternative conjugation, shown in Figure 5.1b, involves applying the SDK operation N times at a de-tuned motional frequency in contrast to the resonant kicks done previously. The time dynamics of the evolution are shown in Figure5.1. Although the $X(\pi/2)$ conjugation is still sensitive to the spin phase of the kick, the overall slopes shown in the different Stark shifts are still present, allowing us to adequately calibrate the combined two tone frequencies.

5.1.3.2 Motional Frequency

Our goal is to emulate Equation 5.30 with spin phase ϕ. The Hamiltonian also describes motional frequency ω, which will act as a detuning element from the BSB and RSB terms derived in Equation 5.3. As such, we need to accurately determine the RSB and BSB frequencies during the SDK operation. Typically, the RSB and BSB transition frequency can be determined by a direct measurement of both the respective RSB and BSB spectrums. In practice, this is done by fixing one Raman laser frequency and scanning the frequency of the second Raman beam. However, such a scan does not emulate the SDK operation, as

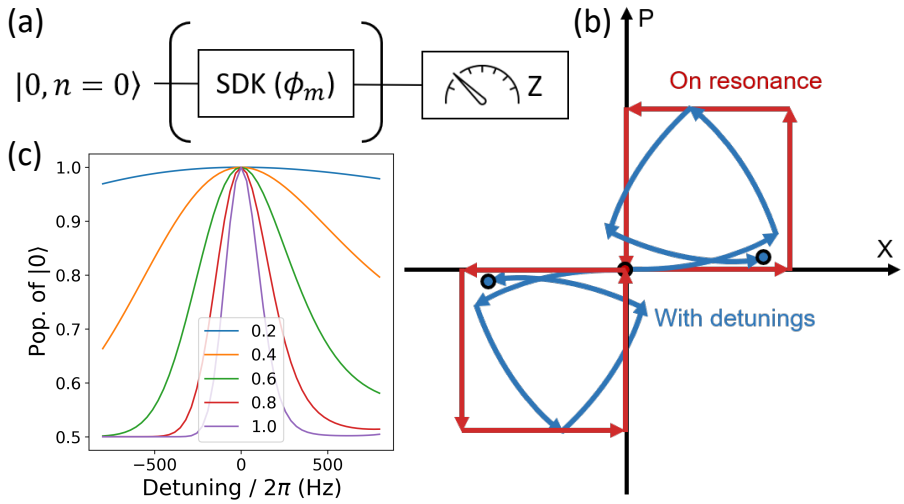

FIGURE 5.3: **Motional Frequency Calibration Method.** a) Circuit model to calibrate the motional frequency. The ion is prepared into a $|0\rangle$ state then undergoes 4 motional kicks, each with a change in motion phase by 90^o. b) Phase diagram of the motional frequency trajectory when each kick is on resonant (red) with the RSB and BSB kicks. If there is any detuning as we scan the motional frequency, the motion will not return to the origin (blue). c) Modeled calibration of the measured population in the Z-basis with respect to the motional frequency detuning.

both RSB and BSB will be used concurrently during the gate. As such, the direct measured transition spectrum will be inaccurate and we needed to devise an alternative method to measure the motional sidebands.

The method we utilized is shown in Figure 5.3a. By initializing the ion in the spin ground state $|0\rangle$ and motion ground state $|n = 0\rangle$ and applying four SDK operations, each with a respective motion change by $\pi/2$, only when the SDK is on resonant will the ion return to a pure state $|0, n = 0\rangle$. Otherwise, when the kicks are detuned, the ion will return to a mixed state, which we can observe in the measured population shown in Figure 5.3c. Furthermore, by increasing the length of the SDK operation, shown in the legend of Figure 5.3c, the scanned linewidth becomes narrower, improving the calibration precision. This method allows us to know the motional frequency precisely and apply our model detuning exactly from the resonant frequency within 100 Hz.

5.1.3.3 Phase Tracking

Now we have established the target dynamics and the Trotterization implementation method, running the LVC model on the trapped-ion simulator requires careful control of the Raman lasers to achieve the desired dynamics. From the operator's perspective, there are essentially two gates that are iterated over, single-qubit (SQ) gates and spin coherent kicks. We illustrate the circuit model in Figure 5.4a for a Trotterized spin coherent kick on one mode and a single qubit gate. As the circuit evolves over the Trotterization, we need to carefully track the Raman laser's phase and synchronize the relative phase to the ion's spin and motion.

In our phase tracking analysis, we synchronize our control RFSoC control system to the SQ carrier frequency. The SQ carrier then becomes the rotating frame for the rest of the circuit. We can achieve this in practice by setting the 355nm repetition rate to match the light shift of the carrier transition. In the absence of any spin-dependent kicks (SDK), the ion's spin phase will remain constant, as shown in the green line of Figure 5.4b. However, the ion's motion is constantly evolving at its own independent frequency, even when no SDKs are applied, shown by the pink linear ion motion curve. Thus, from the moment we start the Trotterization to implement the model, we need to track the ion motion, as shown by the horizontal offset in the pink curve for the first SQ gate in the Trotterization. When we introduce the SDK, the ion's motion phase must match the linear curve for the red sideband (and a corresponding, not shown, negative slope for the blue sideband). When returning to a SQ operation in the Trotterization, the RFSoC is operating at the target frequency, so the phase is reset to zero.

Once we consider the light shifts and motion detuning for the SDKs, the phase tracking plot is adjusted as shown in Figure 5.4c. First, we will consider the SDK light shift. Each time the ion is exposed to the SDK operation, the ion phase is adjusted by the two tone light shift as shown in the slope change on the green curve. Thus, now when returning to an SQ operation, the new shifted phase has to be considered. The light shift manifests as a

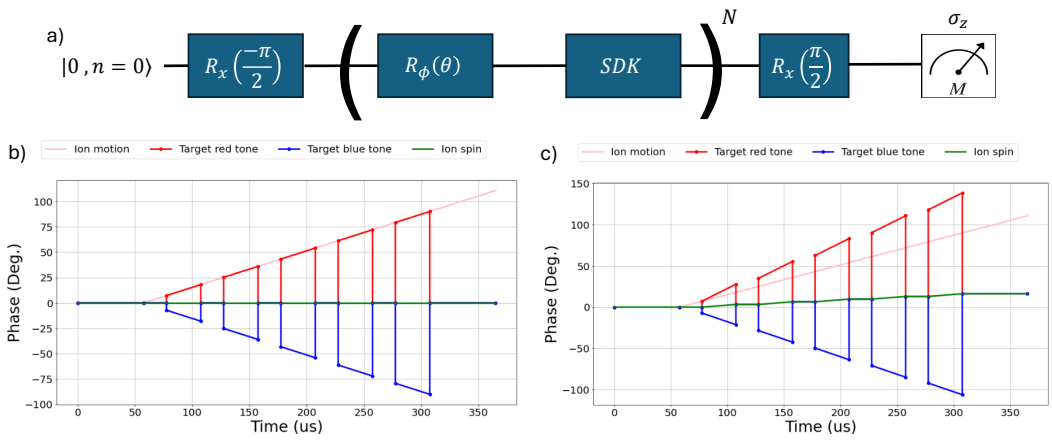

FIGURE 5.4: **Circuit model of LVCM implemented on the trapped ion simulator with phase tracking simulation for 5 trotter steps.** a) Model of LVCM for one SQ gate and one Spin Dependent Kick, Trotterized and repeated N times. The Hamiltonian is first conjugated by $R_x(\pi/2)$ prior to the Trotterization. The final state is measured in the z basis. b) Phase tracking using the carrier SQ frequency as the rotating frame. The ion spin and motion are illustrated when all the operations are driven on resonance and no light shift is accounted for. For this particular example, the number of trotter steps has been set to 5. c) Once we add the light shift from the SDK and add motion detuning to simulate the LVCM, the target red and blue tones have shifted as shown. All values have been exaggerated from actual experimental values to clearly differentiate the operations.

positive linear slope to both red and blue sidebands, so both red and blue phases are shifted symmetrically. Furthermore, during the SDK operation, a motion detuning frequency is added. This acts as an additional slope that is evolved when the SDK is turned on. However, unlike the light shift, the motion detuning acts as an asymmetric slope, positive for the red sideband and negative for the blue sideband. The contribution of all these components in shown for the respective 'Target Red and Blue' phases and the final plot is a representation of how the circuit is implemented in practice.

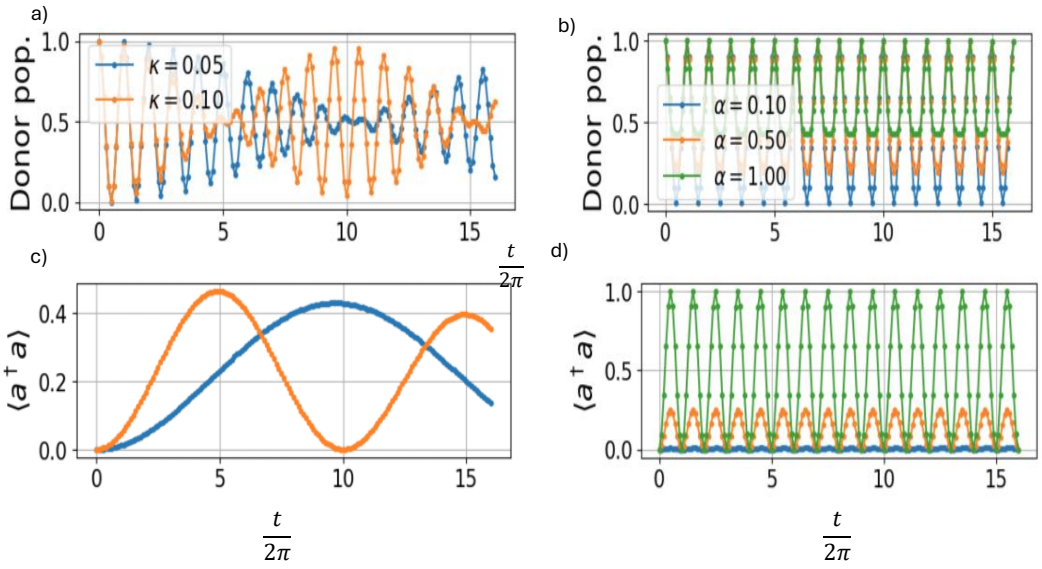

FIGURE 5.5: **Model Expectations of a predominantly x or y kick.** Measurements are shown for both the σ_z bright state operator and the respective phonon number. Nodes in the bright state can adequately be explained by population increases in the phonon number at the same time steps.

5.2 LVC Results

By setting some arbitrary parameters of the LVC model, we can set some expectations of the targeted time evolution. We set this as a benchmark of the Trotterization and calibration procedures we described previously. In this scenario, the time dependence of the parameters shown in Equation 5.29 is omitted for simplicity.

5.2.1 Model Expectations

We will examine the time dynamics primarily of the SDK as the SQ operations are significantly more straight-forward. First, I rewrite Equation 5.29 as

$$H = \frac{\Delta}{2}\hat{\sigma}_x + \frac{\kappa}{2}\hat{\sigma}_y(\hat{b}^\dagger e^{i\nu t} + \hat{b}e^{-i\nu t}) + \frac{\alpha}{2}\hat{\sigma}_x(\hat{b}^\dagger e^{i\nu t} + \hat{b}e^{-i\nu t}) \tag{5.31}$$

for the following model expectations, where the motional frequency for the LVC model is now denoted by ν. By setting the motional detuning, ν, to be 1.0, we obtain the curves

shown in Figure 5.5 with $\Delta = 1.0$. When the SDK and the SQ term are along the same axes, we see a node form in the time dynamics, Figure 5.5a, which correlates to maximum increase in the phonon number $< a^\dagger a >$, Figure 5.5c. When energy is transferred back from the phonon to the spin, the population is fully revived as shown in $T = 10 \times t/2\pi$. In juxtaposition, when the spin-motion coupling occurs on the same axes as the SQ term, it acts as an additional $\hat{\sigma}_x$, changing the spin state by a proportion to its coupling strength α. This aligns with the maximum increase in the phonon number Figure 5.5d at each of the nodes on Figure 5.5b.

These effects can be combined into one SDK operation with an arbitrary spin phase angle ϕ as shown in Equation 5.30. To observe the coupling strength along both axes, the absolute value was set to *0.2* such that $0.2 = 0.2(\cos\theta\sigma_x + \sin\theta\sigma_y)$. This made the contribution along due to the σ_x kick more prominent for visualization. The expected time dynamics are shown in Figure 5.6. This target will be the focus of the next section.

5.2.2 Raman Spin Angle Measurements of SDK

We explore the SDK operation along different Raman spin phases, validating the notion from Equation5.30. By proving this proof of concept, when we run the SDK operation, we can change axes of the effective spin-motion coupling as a function of time. This is critical to demonstrating the Herzberg-Teller effect where the dipole matrix element causes the spin-motion coupling to vary during the time evolution.

First, we explore the two extreme axes of our evolution, where one SDK is along the direction of the SQ gate term and the other is nearly $\pi/2$ shifted. By comparing the measured time dynamics, shown via the scattered points, with the expected evolution at a fitted spin-phase angle, we can see a nice overlap between our intended evolution and our trapped ion simulator's result. In this particular data set, there was some offset in the carrier σ_x term by 4% but this can be easily addressed by a more careful application of our carrier calibration. The correction will be shown and implemented in Figure 5.7.

Second, we further explore our SDK arbitrary angle evolution along two intermediary

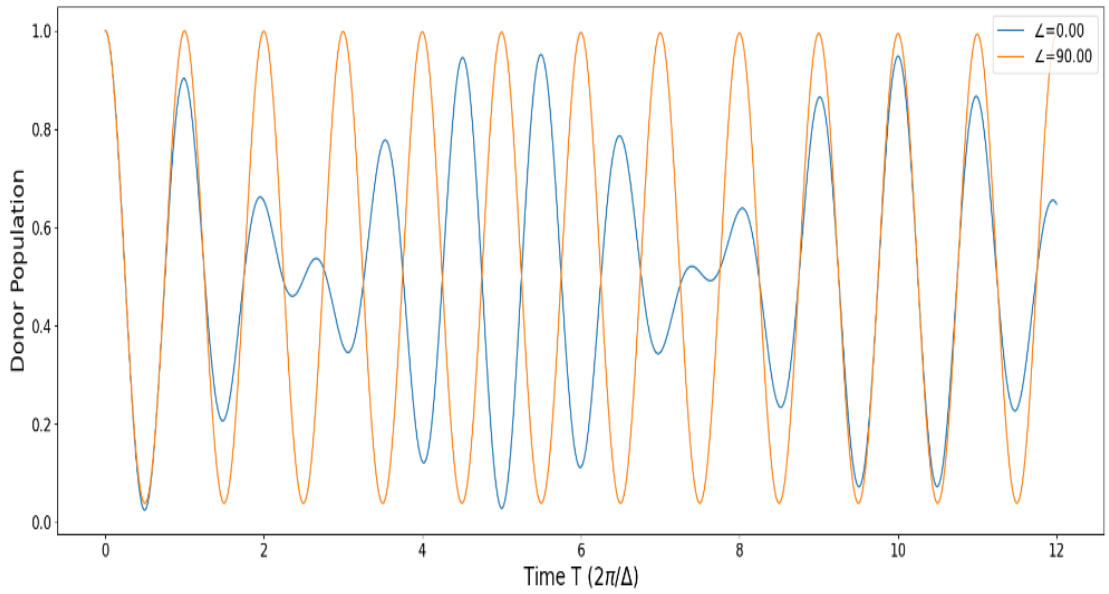

FIGURE 5.6: **Time dynamics of the LVC model depending on the spin angle of the electronic-vibration coupling.** The strength of the coupling has been set to an unit-less 0.2 for this model. At 0 degrees, we see maximum interchange between the electronic states and the vibrational modes. This results in nodes in the electronic state observable at t=3 and 7. At 90 degrees, the motion is acting along the same axes as the SQ term.

axes. This will validate full control of the LVC mapping, and help us predict how our input Raman phase correlates with the expected dynamics. These two evolutions are nearly $\pi/4$ between the exclusively $\hat{\sigma}_x$ and $\hat{\sigma}_y$ spin-motion coupling. Once again, we see a nice overlap between our measured σ_z population and a fitted spin phase angle σ_ϕ. The results are shown in Figure5.8.

Considering all four of these measured dynamic evolutions as a function of our input Raman control phase ϕ, we can see a clear negative correlation between our control and the mapped LVC Hamiltonian. There should be a $abs(1)$ mapping between these two angles, which we see in Figure 5.9. The negative slope is easy to interpret as the Raman spin phase is dependent on the relative phase of the two photons in Figure 2.9. A negative correlation indicates that the control photon we are adjusting is the lower energy photon in our two-Raman set-up.

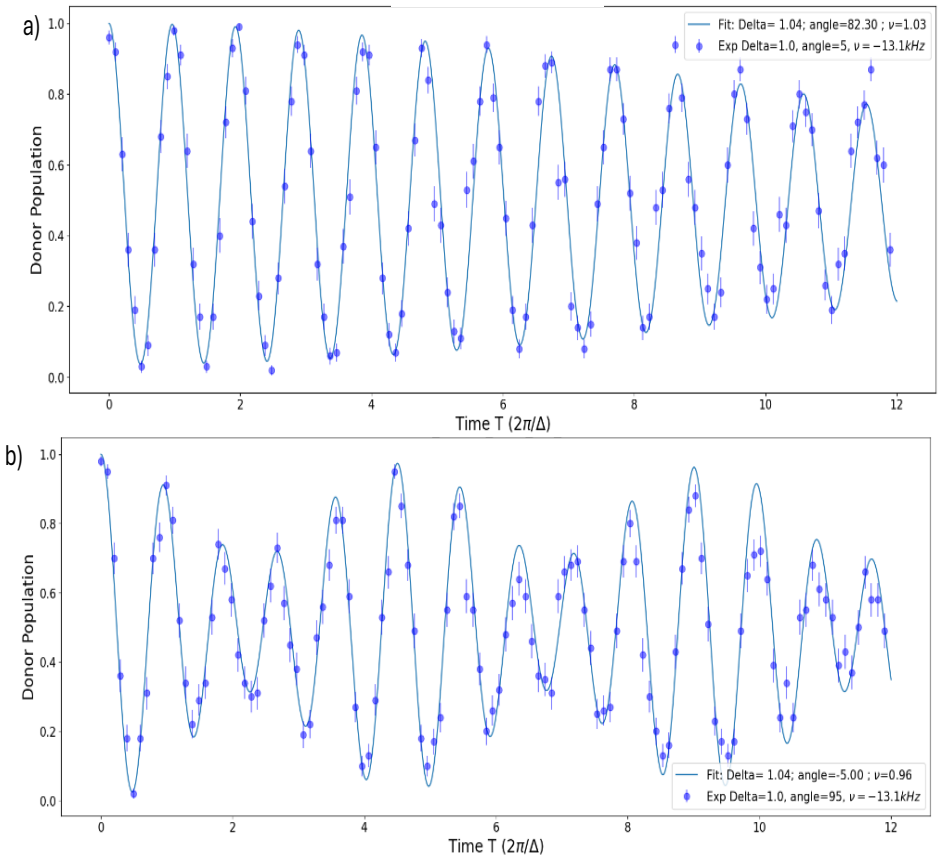

FIGURE 5.7: **Predominant σ_x and σ_y kick evolution.** The evolution on the two extreme axes of the SDK operation. a) Evolution when the kick and the SQ operation are along the same axes. b) The SDK and SQ are along nearly orthogonal axes, leading to the nodes in the spin population as the time evolution is monitored.

5.2.3 Motion Frequency Offset

In the data shown in Figure 5.7 and Figure 5.8, the motion term ν for our LVC Hamiltonian is set to 1.0. We use this value to estimate the motion detuning of the red and blue sidebands, which for our experiment parameters is an asymmetric detuning of *-13.1 kHz* from our RSB and BSB. However, if you inspect the fits shown in these figures, the $\nu! = 1$ and is off from the expected input by $\approx 3-4\%$ in these curves. Furthermore, when we scan the control ν at different frequencies, our expected detuning is consistently off by 400-500 Hz. We suspected an asymmetric frequency is off in our calibration, which is not accounted for in the prior analysis.

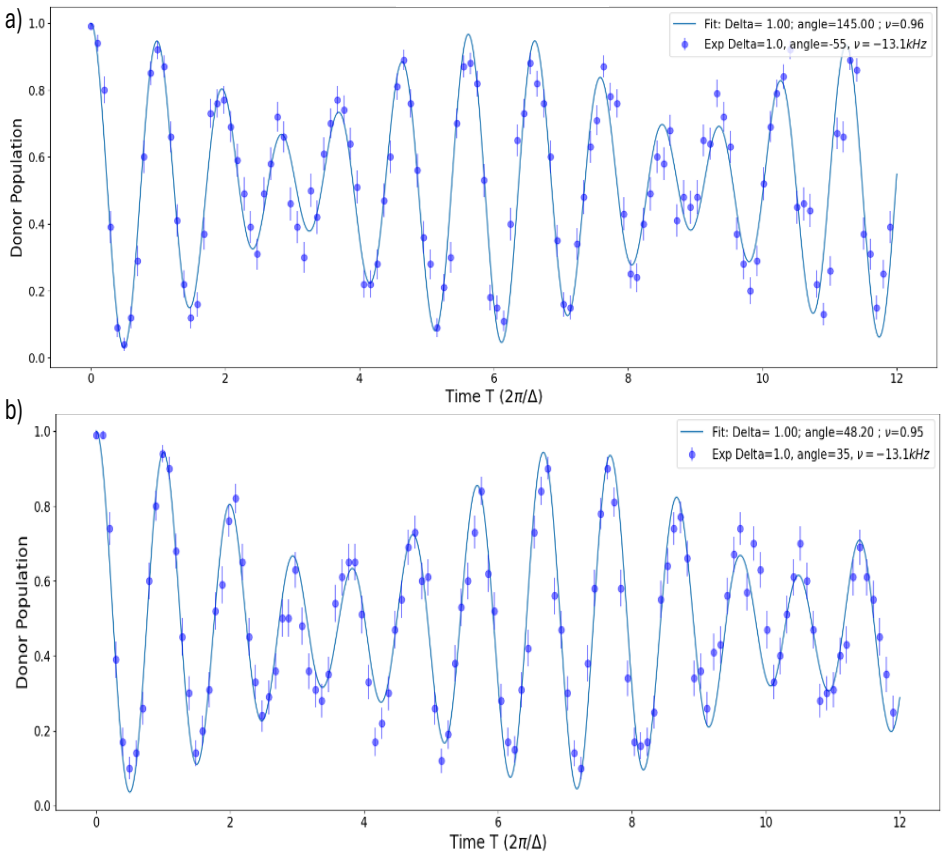

FIGURE 5.8: **Mixed σ_x and σ_y kick evolution.** Between the two primary axes, we run the LVC model. These evolutions can be fitted to an angle a) -55^o, and b) 35^o. Technically these evolutions can also be explained by a rotation at 180^o around the origin.

In principle, the motional frequency should be symmetric about the carrier and we make this assumption when we fit the motional frequency in Section 5.1.3.2. However, in reality this assumption may not be true. At a naive level, the AOM we use to adjust to the red and blue sideband frequencies can have different efficiencies, which can adjust the relative Stark shift of each red and blue tone. However, when we consider the mathematical representation of the fourth-order Stark shift, accounting for the Raman laser's repetition rate, a more fundamental explanation becomes clear.

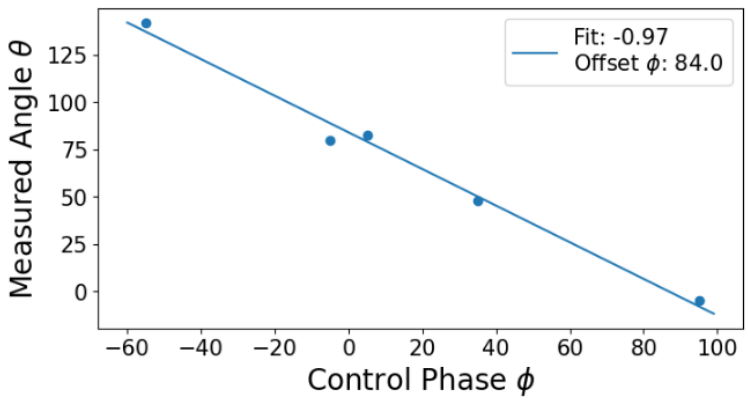

FIGURE 5.9: **The control Raman phase relative to the fitted LVCM model's angle.** By comparing the fitted measured angle dynamics relative to our Raman control parameter, we see a negative 1 correspondence. This indicates the control Raman phase we are adjusting is the lower energy photon in our control. The negative slope matches the frequency for each photon we use in our two photon Raman transition.

5.2.3.1 Fourth Order AC Stark Shift Contributions

From Figures 5.1 and 5.2, it seemed that we had already tracked down all the relevant Stark shifts and calibrated the value within 100 Hz. However, these calibrations limit us to symmetric shifts in the red and blue sideband frequencies. If there is any asymmetry in the Stark shift, it would not be captured by these scans. The fourth order Stark shift, when considering the frequency comb of the 355 nm laser, can describe this asymmetry. First we write the general expression for 4th-order Stark shift

$$\Delta E^{(4)} = P^2 I_1 I_2 K_{ij} \tag{5.32}$$

where

$$K_{ij} \equiv \sum_k \left(\frac{k\omega_{rep}t}{2}\right)^2 \operatorname{csch}^2 \frac{k\omega_{rep}t}{2} \cdot \left(\frac{1}{k\omega_{rep} - \omega_{ij} + \delta\omega_{comb}} + \frac{1}{k\omega_{rep} - \omega_{ij} - \delta\omega_{comb}}\right) \tag{5.33}$$

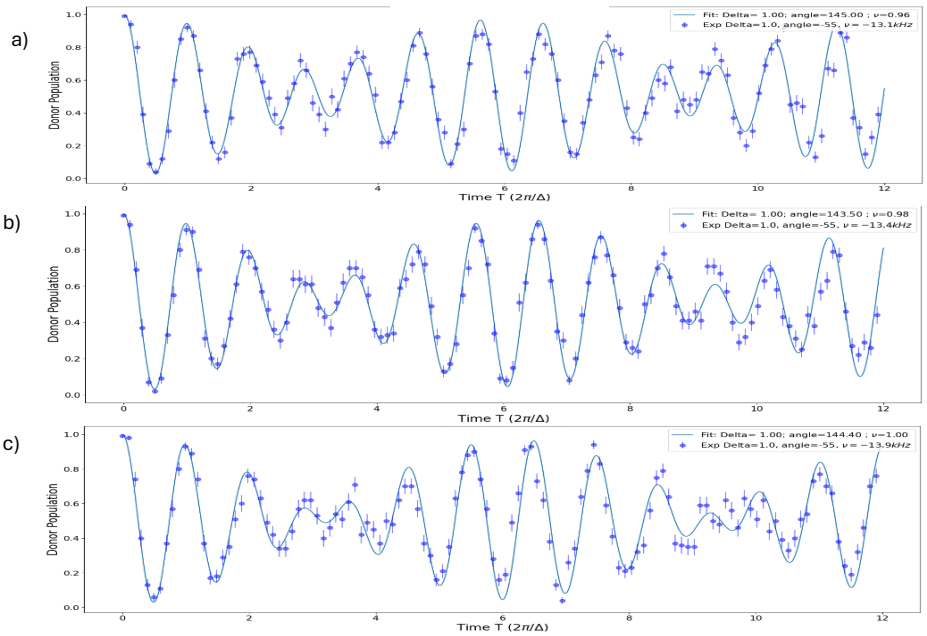

FIGURE 5.10: **Scanning the motional detuning for the Linear Vibronic Coupling Model.** By adjusting the detuning in the simulator, we can emulate different ν. The model fits well for an arbitrary $\nu = 0.96(a), .96(b) and 1.0(c)$.

P represents the polarization of each photon, and I_i is the respective intensity of each laser. [Kyprianidis, 2021]

When the frequency comb drives the hyperfine transition of Ytterbium ω_{HF}, the following condition is satisfied

$$\left|f_A + n f_{rep}\right| = \omega_{HF}/2\pi \tag{5.34}$$

where $2\pi f_A$ is the frequency difference between the control AOMs and n is an integer. Parameterizing the repetition rate frequency with

$$x \equiv \frac{\frac{\omega_0}{2\pi} mod f_{rep}}{f_{rep}} \tag{5.35}$$

simplifies Equation 5.34 to $f_A = (k \pm x) f_{rep}$. This gives the total Stark shift from Equation 5.32 to be

$$\Delta E^{(4)} = P^2 I_1 I_2 \sum_k h_k^2 \frac{1}{k - n - x + f_A/f_{rep}} + \frac{1}{k - n - x - f_A/f_{rep}} \tag{5.36}$$

where $h_k = (\frac{k\omega_{rep}t}{2})\,\mathrm{csch}\,\frac{k\omega_{rep}t}{2}$.

Under the condition of the SDK, the red and blue sideband frequencies follow the condition $f_{Ab} - f_{Ar} = kf_{rep} \pm 2f_M$ where f_M is the motional mode frequency. The relative shift between the two modes can then be expressed as

$$\Delta E^{SDK} = \mathcal{P} I_1 I_2 \Delta E_0 (\alpha \mathcal{E}(x, xf_{rep} + f_M) + \alpha^{-1} \mathcal{E}(x, xf_{rep} + f_M)) \tag{5.37}$$

where the $\mathcal{E}$ is the comb function,

$$\mathcal{E}(x, f_A) = \frac{1}{2} \sum_k h_k^2 \left(\frac{1}{k - n - x + f_A/f_{rep}} + \frac{1}{k - n - x - f_A/f_{rep}}\right) \tag{5.38}$$

$\mathcal{P}$ is a polarization factor from the two Raman beams, α is a dimensionless value expressing the imbalance between the blue and red tone intensities $\alpha \equiv \sqrt{I_b/I_r}$, and I_i is the respective intensity for each photon in the Raman transition. The base Stark shift ΔE_0 is defined by the Rabi frequency which is independent of the experimental parameters and can be written as

$$\Delta E_0 \equiv -\frac{\Omega_{1,2}}{P^2 I_1 I_2 2\pi f_{rep}} \tag{5.39}$$

A more detailed derivation can be found in [**Euriqua**].

A zoomed in plot of the fourth order stark shift Equation 5.37 is shown in Figure 5.11 with relevant experimental parameters. In the Figure, the two red and blue frequency tones we drive for the SDK have been estimated roughly at 2 MHz. The key takeaway from this is for both tones in the coherent kick, there is a positive shift in the frequency. Typically, the repetition rate for the 355 nm is tuned such that the red and blue tones are asymmetric about zero, nullifying the AC stark shift. Unfortunately, our experimental configuration does not have this capability. The difference between the tones is about 600 Hz, nearly identical to the 400-500 Hz estimated from our data in Figure 5.10 and poses a likely candidate for the measured offset.

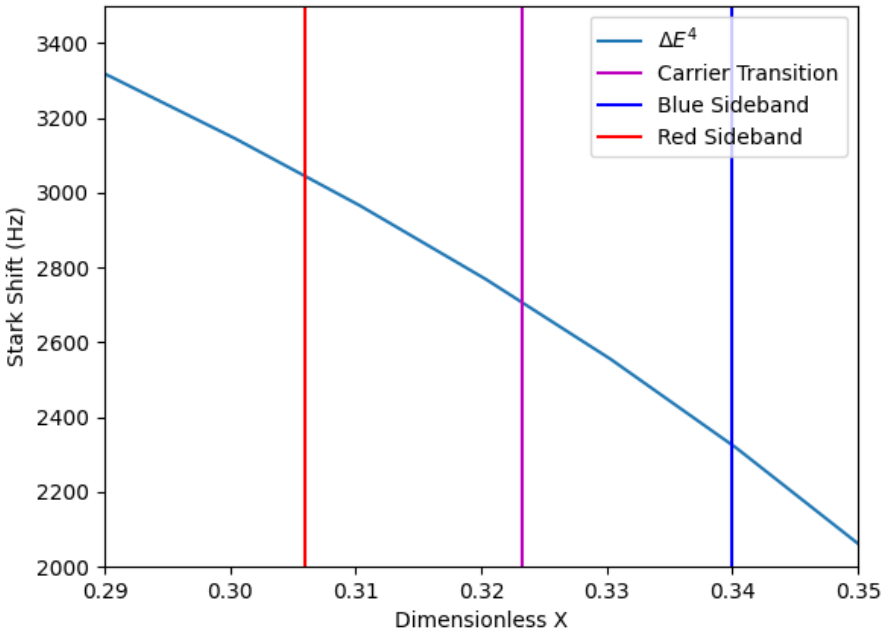

FIGURE 5.11: **Fourth Order Stark Shift (Equation 5.37) for the Carrier Transition, red sideband and blue sideband transition.** The function assumes a 31 ps pulse time, repetition rate of 117.8 MHz, Rabi Frequency of 100 kHz, 2MHz offsets for red and blue tones, and the power balanced between red and blue tones ($\alpha = 1$).

5.2.3.2 Proposed Solution

The easiest solution to address this problem is to make the repetition rate tunable for the 355 nm, as shown in Figure 5.12. This can be done by setting the repetition rate to 119.6 MHz, then the red and blue sidebands' respective stark shifts will be symmetric around the carrier transition, and the asymmetry will be nullified.

If this solution is not possible, due to hardware limitations, then another solution is to characterize the fluctuation in the fourth-order contributions and their relative time scale. Stark shift is susceptible to polarization changes, intensity noise, and beam pointing noise relative to the ion. If these fluctuations are small relative to the time scale of our Herzberg-Teller model, then the offset needs to be measured only before running the circuit. Then the stark shift can be predicted based off the motional frequency, and Equation 5.37.

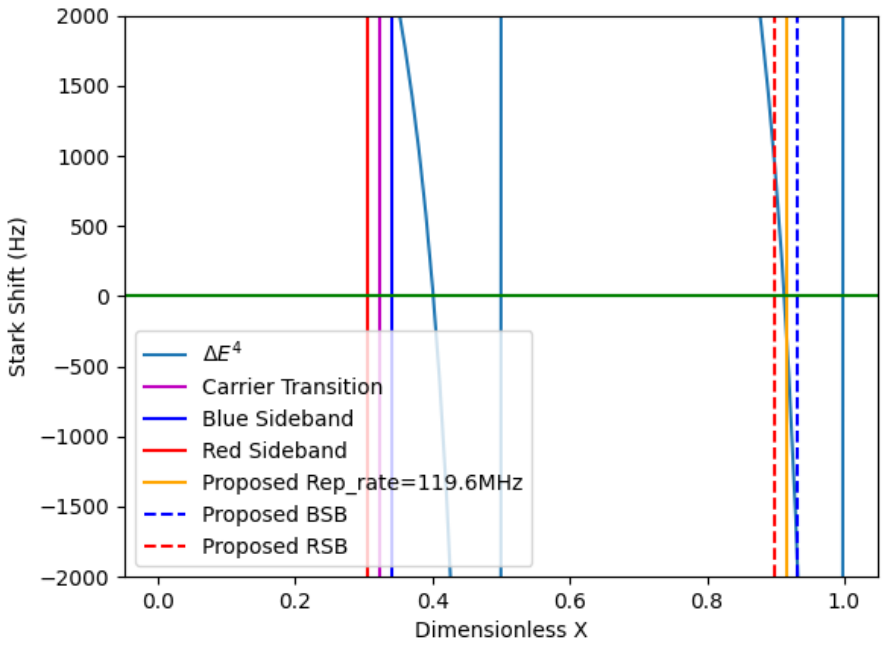

FIGURE 5.12: **Proposed repetition rate to address fourth order AC Stark shift.** Current location is referred to as the carrier transition with the respective red and blue sidebands. The proposed location is shown in orange, with the following moved red and blue sidebands shown via dashed lines.

5.3 Future Steps

The work here sets the framework for running the Herzberg-Teller model and identifies the key calibrations needed to obtain meaningful results. The next logical steps are to use all the tools we have described, account for the Stark shifts appropriately, and run the time dynamics of Equation 5.29. By analyzing the frequency components in the evolution, we can derive the electronic spectra for some metal-based tetrapyrolle derivatives outlined in Roy et al., 2022. This model is ideal because there are only three modes in the molecule to target, which align with the three motional modes the center ion couples to in our trapped ion chain. As longer ion chains are incorporated, more sophisticated molecules can be targeted. In addition, we limit our models to one electronic spin. By adding a two qubit Molmer-Sorensen gate, which we already demonstrated on the system, models including proton transfer [Polyak et al., 2015] unusual Stokes shift [Galiana and Lasorne, 2023] can

also be simulated.

6. Conclusions

In this thesis, we have looked at the fundamental tools to perform ion trapping and perform novel quantum simulations. We looked at the chemical model, known as the linear vibronic coupling model, and demonstrated working dynamics on our trapped ion simulator that matches with expected Hamiltonian evolution. We provided the tools necessary to achieve this quantum simulation, including but not limited to phase tracking the RF pulses of our Raman lasers, adequately accounting for light shift as we move from one-tone to two-tone operations, and accurately identifying our motional sideband frequencies.

We then examined an effect unaccounted for in our calibrations, the fourth-order Stark shift, and examined how it may be affecting our mapped Hamiltonian. Although not verified in experimental data, we estimated the contribution of this term, and found it to be of a similar scale to offsets we were seeing in our model. We propose methods to address this issue for future experimentalists looking to expand on our work.

Furthermore, we explore the efficacy of integrating an optical cavity with a trapped ion system. We analyze the noise that came from our cantilever design. We demonstrate coupling, despite the flawed design between input light and the cavity in question. In addition, we provide a novel method to fabricate micromirrors to be used with atomic cavities and describe numerous methods to quantify the surface quality.

Bibliography

Aikyo, Y., Vrijsen, G., Noel, T. W., Kato, A., Ivory, M. K., & Kim, J. (2020). Vacuum characterization of a compact room-temperature trapped ion system. *Applied Physics Letters*, *117*(23), 234002. https://doi.org/10.1063/5.0029236

Anonymous. (1926). Minutes of the stanford meeting, march 6, 1926. *Phys. Rev.*, *27*, 637–644. https://doi.org/10.1103/PhysRev.27.637

Balzer, C., Braun, A., Hannemann, T., Paape, C., Ettler, M., Neuhauser, W., & Wunderlich, C. (2006). Electrodynamically trapped Yb^+ ions for quantum information processing. *Phys. Rev. A*, *73*, 041407. https://doi.org/10.1103/PhysRevA.73.041407

Barnes, W. L., Horsley, S. A. R., & Vos, W. L. (2020). Classical antennas, quantum emitters, and densities of optical states. *Journal of Optics*, *22*(7), 073501. https://doi.org/10.1088/2040-8986/ab7b01

Bernien, H., Schwartz, S., Keesling, A., & et al. (2017). Probing many-body dynamics on a 51-atom quantum simulator. *Nature*, *551*(7682), 579–584. https://doi.org/10.1038/nature24471

Binnig, G., Quate, C. F., & Gerber, C. (1986). Atomic force microscope. *Phys. Rev. Lett.*, *56*, 930–933. https://doi.org/10.1103/PhysRevLett.56.930

Bowers, C. J., Budker, D., Commins, E. D., DeMille, D., Freedman, S. J., Nguyen, A.-T., Shang, S.-Q., & Zolotorev, M. (1996). Experimental investigation of excited-state lifetimes in atomic ytterbium. *Phys. Rev. A*, *53*, 3103–3109. https://doi.org/10.1103/PhysRevA.53.3103

Brown, K., Kim, J., & Monroe, C. (2016). Co-designing a scalable quantum computer with trapped atomic ions. *2*. https://doi.org/10.1038/npjqi.2016.34

Cui, G., & Raymer, M. G. (2005). Quantum efficiency of single-photon sources in the cavity-qed strong-coupling regime. *Opt. Express*, *13*(24), 9660–9665. https://doi.org/10.1364/OPEX.13.009660

Debnath, S. (2016). *A programmable five qubit quantum computer using traped atomic ions* [Doctoral dissertation, University of Maryland].

Devoret, M. H., & Schoelkopf, R. J. (2013). Superconducting qubits: A short review. *Physics Today*, *56*(5), 38–44. https://doi.org/10.1063/PT.3.2023

Dill, K. A., & MacCallum, J. L. (2012). The protein-folding problem, 50 years on. *Science*, *338*(6110), 1042–1046. https://doi.org/10.1126/science.1219021

DiVincenzo, D. P. (2000). The physical implementation of quantum computation. *Fortschritte der Physik*, *48*(9–11), 771–783. https://doi.org/10.1002/1521-3978(200009)48:9/11<771::aid-prop771>3.0.co;2-e

Egan, L., Debroy, D. M., Noel, C., Risinger, A., Zhu, D., Biswas, D., Newman, M., Li, M., Brown, K. R., Cetina, M., & Monroe, C. (2021). Fault-tolerant control of an error-corrected qubit. *Nature*, *598*, 281–286. https://doi.org/10.1038/s41586-021-03928-y

Einstein, A., Podolsky, B., & Rosen, N. (1935). Can quantum-mechanical description of physical reality be considered complete? *Physical Review*, *47*(10), 777–780. https://doi.org/10.1103/PhysRev.47.777

et al., T. (2024). *https://arxiv.org/pdf/2409.04044*.

Euriqa. (Accessed 2024). Stark shift nulling. *Internal Euriqa Memo*.

Feynman, R. P. (1982). Simulating physics with computers. *International journal of theoretical physics*, *21*(6/7), 467–488.

Fox, A., & Li, T. (1963). Modes in a maser interferometer with curved and tilted mirrors. *Proceedings of the IEEE*, *51*(1), 80–89. https://doi.org/10.1109/PROC.1963.1663

Francs, G. C. d., Barthes, J., Bouhelier, A., Weeber, J. C., Dereux, A., Cuche, A., & Girard, C. (2016). Plasmonic purcell factor and coupling efficiency to surface plasmons. implications for addressing and controlling optical nanosources. *Journal of Optics*, *18*(9), 094005. https://doi.org/10.1088/2040-8978/18/9/094005

Galiana, J., & Lasorne, B. (2023). On the unusual stokes shift in the smallest ppe dendrimer building block: Role of the vibronic symmetry on the band origin? *The Journal of Chemical Physics*, *158*(12), 124113. https://doi.org/10.1063/5.0141352

Gavrila, R., Dinescu, A., & Mardare, D. (2006). Afm applications to the study of thin films morphology: A power spectral density approach. *2006 International Semiconductor Conference*, *1*, 167–170. https://doi.org/10.1109/SMICND.2006.283959

Haljan, P. C., Brickman, K.-A., Deslauriers, L., Lee, P. J., & Monroe, C. (2005). Spin-dependent forces on trapped ions for phase-stable quantum gates and entangled states of spin and motion. *Phys. Rev. Lett.*, *94*, 153602. https://doi.org/10.1103/PhysRevLett.94.153602

Harty, T. P., Allcock, D. T. C., Ballance, C. J., Guidoni, L., Janacek, H. A., Linke, N. M., Stacey, D. N., & Lucas, D. M. (2014). High-fidelity preparation, gates, memory, and readout of a trapped-ion quantum bit. *Phys. Rev. Lett.*, *113*, 220501. https://doi.org/10.1103/PhysRevLett.113.220501

Harvey, J. E., Choi, N., Schroeder, S., & Duparré, A. (2012). Total integrated scatter from surfaces with arbitrary roughness, correlation widths, and incident angles. *Optical Engineering*, *51*(1), 013402. https://doi.org/10.1117/1.OE.51.1.013402

Hoogenboom, B. W., Hug, H. J., Pellmont, Y., Martin, S., Frederix, P. L. T. M., Fotiadis, D., & Engel, A. (2006). Quantitative dynamic-mode scanning force microscopy in liquid. *Applied Physics Letters*, *88*(19), 193109. https://doi.org/10.1063/1.2202638

Jia, Z., Wang, Y., Zhang, B., Whitlow, J., Fang, C., Kim, J., & Brown, K. R. (2022). Determination of multimode motional quantum states in a trapped ion system. *Phys. Rev. Lett.*, *129*, 103602. https://doi.org/10.1103/PhysRevLett.129.103602

Kano, H., Saito, T., & Kobayashi, T. (2002). Observation of herzberg–teller-type wave packet motion in porphyrin j-aggregates studied by sub-5-fs spectroscopy. *The Journal of Physical Chemistry A*, *106*(14), 3445–3453. https://doi.org/10.1021/jp012493f

Khan, M., Wang, Q., & Fitzpatrick, M. (2016). 1 - atomic force microscopy (afm) for materials characterization. In G. Hübschen, I. Altpeter, R. Tschuncky, & H.-G. Herrmann (Eds.), *Materials characterization using nondestructive evaluation (nde) methods* (pp. 1–16). Woodhead Publishing. https://doi.org/https://doi.org/10.1016/B978-0-08-100040-3.00001-8

Kraft, S., Deninger, A., Trück, C., Fortágh, J., Lison, F., & Zimmermann, C. (2004). Rubidium spectroscopy at 778–780 nm with a distributed feedback laser diode. *Laser Physics Letters*, *2*(2), 71. https://doi.org/10.1002/lapl.200410155

Kundu, S., Roy, P. P., Fleming, G. R., & Makri, N. (2022). Franck–condon and herzberg–teller signatures in molecular absorption and emission spectra [PMID: 35389662]. *The Journal of Physical Chemistry B*, *126*(15), 2899–2911. https://doi.org/10.1021/acs.jpcb.2c00846

Kyprianidis, A. (2021). *Simulating many body quantum spin models with trapped ions* [Doctoral dissertation, University of Maryland].

Law, C. K., & Kimble, H. J. (1997). Deterministic generation of a bit-stream of single-photon pulses. *Journal of Modern Optics*, *44*(11-12), 2067–2074. https://doi.org/10.1080/09500349708231869

Leggett, A. J., Chakravarty, S., Dorsey, A. T., Fisher, M. P. A., Garg, A., & Zwerger, W. (1987). Dynamics of the dissipative two-state system. *Rev. Mod. Phys.*, *59*, 1–85. https://doi.org/10.1103/RevModPhys.59.1

Nielsen, M. A., & Chuang, I. L. (2010). *Quantum computation and quantum information* (10th). Cambridge University Press.

Noek, R., Vrijsen, G., Gaultney, D., Mount, E., Kim, T., Maunz, P., & Kim, J. (2013). High speed, high fidelity detection of an atomic hyperfine qubit. *Opt. Lett.*, *38*(22), 4735–4738. https://doi.org/10.1364/OL.38.004735

Nowak, K. M., Baker, H. J., & Hall, D. R. (2006). Efficient laser polishing of silica micro-optic components. *Appl. Opt.*, *45*(1), 162–171. https://doi.org/10.1364/AO.45.000162

Olmschenk, S., Younge, K. C., Moehring, D. L., Matsukevich, D. N., Maunz, P., & Monroe, C. (2007). Manipulation and detection of a trapped Yb^+ hyperfine qubit. *Phys. Rev. A*, *76*, 052314. https://doi.org/10.1103/PhysRevA.76.052314

Paul, W. (1990). Electromagnetic traps for charged and neutral particles. *Rev. Mod. Phys.*, *62*, 531–540. https://doi.org/10.1103/RevModPhys.62.531

Polyak, I., Allan, C. S. M., & Worth, G. A. (2015). A complete description of tunnelling using direct quantum dynamics simulation: Salicylaldimine proton transfer. *The Journal of Chemical Physics*, *143*(8), 084121. https://doi.org/10.1063/1.4929478

Purcell, E. M. (1946). Spontaneous Emission Probabilities at Radio Frequencies. *Physical Review*, *69*, 681. https://doi.org/10.1103/PhysRev.69.674.2

Revelle, M. (2020). *https://arxiv.org/pdf/2009.02398*.

Roy, P. P., Kundu, S., Makri, N., & Fleming, G. R. (2022). Interference between franck–condon and herzberg–teller terms in the condensed-phase molecular spectra of metal-based tetrapyrrole derivatives [PMID: 35929598]. *The Journal of Physical Chemistry Letters*, *13*(32), 7413–7419. https://doi.org/10.1021/acs.jpclett.2c01963

Saleh, B., & Teich, M. (2007). *Fundamentals of photonics*. John Wiley & Sons, Inc.

Scully, M., & Zubairy, M. (1997). *Quantum optics*. Cambridge University Press.

Siverns, J., Simkins, L., S.Weidt, & Hensinger, W. (2012). *Applied Physics B*, *107*, 921–934.

Stover, J. C. (1995). *Optical scattering, measurement and analysis 2nd ed.* SPIE - The International Society for Optical Engineering.

Sträng, J. E. (2007). On the characteristic exponents of floquet solutions to the mathieu equation. https://arxiv.org/abs/math-ph/0510076

Sun, K. (2024). *Quantum simulation of electron transfer dynamics using a trapped-ion system* [Doctoral dissertation, Duke University].

Sun, K., Fang, C., Kang, M., Zhang, Z., Zhang, P., Beratan, D. N., Brown, K. R., & Kim, J. (2023). Quantum simulation of polarized light-induced electron transfer with a trapped-ion qutrit system [PMID: 37358521]. *The Journal of Physical Chemistry Letters*, *14*(26), 6071–6077. https://doi.org/10.1021/acs.jpclett.3c01166

Teller, M., Messerer, V., Schüppert, K., Zou, Y., Fioretto, D. A., Galli, M., Holz, P. C., Reichel, J., & Northup, T. E. (2023). Integrating a fiber cavity into a wheel trap for strong ion–cavity coupling. *AVS Quantum Science*, *5*(1), 012001. https://doi.org/10.1116/5.0121534

Vrijsen, G., Aikyo, Y., Spivey, R. F., Inlek, I. V., & Kim, J. (2019). Efficient isotope-selective pulsed laser ablation loading of $^{174}Yb^{+}$ ions in a surface electrode trap. *Opt. Express*, *27*(23), 33907–33914. https://doi.org/10.1364/OE.27.033907

Wang, P., Luan, C.-Y., Qiao, M., Um, M., Zhang, J., Wang, Y., Yuan, X., Gu, M., Zhang, J., & Kim, K. (2021). *Nature Communications*, *12*. https://doi.org/10.1038/s41467-020-20330-w

Wang, Y., Crain, S., Fang, C., Zhang, B., Huang, S., Liang, Q., Leung, P. H., Brown, K. R., & Kim, J. (2020). High-fidelity two-qubit gates using a microelectromechanical-system-based beam steering system for individual qubit addressing. *Phys. Rev. Lett.*, *125*, 150505. https://doi.org/10.1103/PhysRevLett.125.150505

Wu, Q., Shi, Y., & Zhang, J. (2023). Continuous raman sideband cooling beyond the lamb-dicke regime in a trapped ion chain. *Phys. Rev. Res.*, *5*, 023022. https://doi.org/10.1103/PhysRevResearch.5.023022

Zhang, B. (2021). *Improving circuit performance in a trapped-ion quantum computer* [Doctoral dissertation, Duke University].